Investigating the Mechanism of High Temperature Superconductivity by Oxygen Isotope Substitution

Eran Amit

Investigating the Mechanism of High Temperature Superconductivity by Oxygen Isotope Substitution

Research Thesis

In Partial Fulfillment of the
Requirements for the
Degree of Doctor of Philosophy

Eran Amit

Submitted to the Senate of the Technion - Israel Institute of Technology
Shebat 5771 HAIFA January 2011

The Research Thesis Was Done Under The Supervision of Prof.
Amit Keren
in the Faculty of Physics

*A*cknowledgements

I am grateful to Amit Keren for his excellenct guidance.
Thanks to all the "corridor members" and especially Oren, Rinat and Yuval who guided me at my first scientific steps.
It is a pleasure to thank my parents for all the encouragement and support over the years.
I owe my deepest gratitude to my wife Calanit, for all her love and help which made this work possible.

The Generous Financial Help of the Technion is Gratefully Acknowledged

Contents

List of Figures

Abstract

The phenomenon of high temperature superconductivity, discovered in cuprates more than 20 years ago, attracts many experimental and theoretical efforts. Common properties in the phase diagrams and other physical properties of dozens of compounds suggest that the mechanism of superconductivity in all cuprates is the same. One of the big challenges is isolating the properties related directly to superconductivity from the unique material properties. In this work we approach this challenge by measuring the physical response of materials to relatively small chemical changes. We show that these perturbations are small enough and therefore the change in the physical properties can be attributed to small changes in the Hamiltonian describing the system.

In the first part of this work we explore the critical doping variations in cuprates. These are the doping levels at which the compound ground state changes its nature (from an antiferromagnet to a spin glass to superconductor to metal), and they were found to be non-universal. We investigate the origin of these variations by measuring the in-plane oxygen p_σ hole density in the CuO_2 layers as a function of the oxygen density y in $(Ca_xLa_{1-x})(Ba_{1.75-x}La_{0.25+x})Cu_3O_y$ (CLBLCO). This is done using the oxygen 17 nuclear quadrupole resonance parameter ν_Q. We compare compounds with $x = 0.1$ and 0.4 which have significant critical y variations and find that these variations can be explained by a change in the efficiency of hole injection into the p_σ orbital.

The second part of this work is the measurement of the way oxygen isotope substitution affects the Néel temperature. Since isotope substitution is probably the smallest perturbation that can be applied in condensed matter physics its results

are expected to provide strong experimental constrains on superconductivity theories. We choose to measure the isotope effect in $(Ca_{0.1}La_{0.9})(Ba_{1.65}La_{0.35})Cu_3O_y$ which allows to exclude the contribution of a change in the number of holes to the effect. We use μSR and find the absence of oxygen isotope effect on the Néel temperature.

Our first finding, that the critical doping levels are global when the right physical parameter is used, has two direct implementations. The first conclusion is that fictitious effects can be caused if the doping is described by non-physical parameter (for example- the chemical parameter of cation number in the molecular formula). This conclusion is also common to our isotope effect measurement: The isotope effect in cuprates can be described as a change in the number of holes, and therefore should not be used to explain the superconductivity mechanism.

The second implementation comes from a better understanding of the CLBLCO phase diagram. In the transition from four distinct phase diagrams into one universal curve we use only measured parameters. The scaling process shows that the maximum T_c is determined by the planar antiferromagnetic energy scale of the parent compound.

Symbols

SC	Superconductivity
HTSC	Hign temperature superconductor
AFM	Antiferromagnet
SG	Spin glass
PG	Pseudogap
T_c	Critical SC transition temperature
T_N	Critical AFM transition temperature
T_G	Critical SG transition temperature
T^*	Pseudogap cross over temperature
LSCO	$La_{2-x}Sr_xCuO_4$
YBCO	$YBa_2Cu_3O_y$
BVS	Bond valance summation
CLBLCO	$(Ca_xLa_{1-x})(Ba_{1.75-x}La_{0.25+x})Cu_3O_y$
NMR	Nuclear magnetic resonance
ppm	Parts per million
EFG	Electric field gradient
μSR	Muon spin rotation
XFS	X-ray fine structure
OIE	Oxygen isotope effect
rrf	Rotating reference frame
FID	Free induction decay
FFS	Frequency-shifted and summed Fourier transform

Chapter 1

Introduction

1.1 The cuprate superconductors

1.1.1 Superconductivity

Superconductors are materials which below a certain temperature have a phase transition into a state characterized by two important properties: They have absolutely no electric resistance, and they expel magnetic fields. This phase transition has been observed since the beginning of the 20th century in many elements and materials. The transition has taken place in a range of temperatures, the highest reaching about 45 degrees Kelvin. In 1957 Bardeen, Cooper and Schrieffer published their theory [1] of superconductivity. During the 80's of last century new materials were discovered called copper oxide high T_c superconductors (cuprates) [2]. In these materials the critical temperature can be higher than the conventional SC. Today we know about materials with a T_c of about 140K (under pressure)[3]. The cuprates have many other properties which are different from conventional SC, besides having a higher critical temperature. This causes people to believe they have a different mechanism responsible for superconductivity- but this mechanism is still unknown. In order to solve this mystery many experiments were

done over the past three decades, and in the process many new techniques were developed and new HTSC found and explored.

1.1.2 Cuprates phase diagram

The cuprate superconductors are ensemble of dozens of HTSC which have some common properties. The basic character of these materials is the existence of copper oxygen planes in their unit cell. The number of these planes changes between the different cuprates. The oxidation number of the atoms in the CuO_2 can be controlled by changing the molecular formula (this process is called "doping"). Doping changes the chemical and physical properties of the material. Most of the compounds are doped by adding holes ("P type"), while some are doped by electrons ("N type"); we shall not discuss them from now on. There are several critical doping levels in the phase diagram of the cuprates at which the ground state changes (see Fig. 1.1). The first critical doping level is when the long range antiferromagnetic order of the undoped parent compound is destroyed and replaced by a spin glass state; next superconductivity emerges; then the spin glass is destroyed; and finally, superconductivity is destroyed and replaced by a metallic state. These critical levels exist in the phase diagram of all cuprates which can be doped over a wide range such as $La_{2-x}Sr_xCuO_4$ and $YBa_2Cu_3O_y$, but they vary between compounds. The cuprates phase diagram is even more complicated and includes other phases (like the pseudogap), and it is still under investigation. Several attempts have been made to construct a universal phase diagram [4, 5, 6, 7, 8] but thus far only partial diagrams, of only one or two phases, have been achieved.

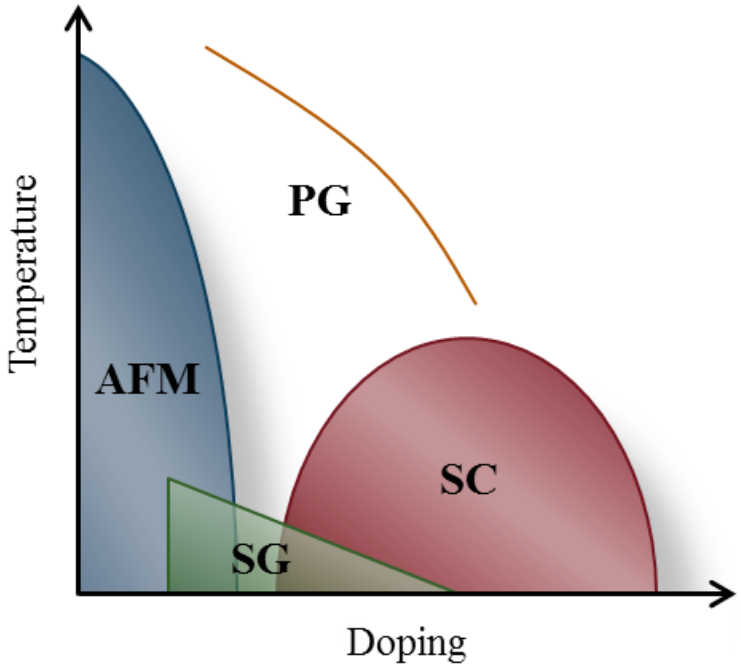

FIGURE 1.1: Typical cuprates phase diagram

1.1.3 Quantification of the doping process

In order to describe the doping process qualitatively, the material can be described as planes of CuO_2 linked to a charge reservoir. The chemical potential of the electrons in the plane is equal to the reservoir's chemical potential. When the reservoir ingredients are changed (the molecular formula is changed), the number of holes in the reservoir is changed, and as a result- the number of holes in the planes is changed. There are two ways to change the number of holes in the reservoir: addition of oxygen atoms (which induce holes, like in YBCO) or changing the cations composition (different cations have different oxidation levels, like in LSCO). The doping process is very difficult to described quantitatively because it involves many different electronic orbitals and energies even in the tight-binding approximation. The LSCO unit cell contains only one CuO_2 plane surrounded by cations and oxygen atoms. Under the assumption that the oxidation level of oxygen is always -2, the number of holes per CuO_2 is directly calculated from the distributions of the La and Sr (the oxidation level of La is +3, Sr is +2). Tallon *et al.* [9] calculated

the number of holes using bond valance summation technique. They concluded that the number of holes per CuO_2 in optimally doped YBCO is 0.16, the same as LSCO. They also proposed a scaling formula for T_c vs. number of holes [10]:

$$1 - T_c/T_c^{max} = 82.6(p - 0.16)^2 \tag{1.1}$$

where p is the hole concentration per CuO_2. The above semi-empirical formula describes successfully many different cuprates, and therefore it was accepted that the optimal doping is about 0.16 holes per CuO_2.

Early experimental works in cuprates showed that in the doping process holes go primary to the oxygens (for example [11]). Eventhough the holes are induced in several different atomic orbitals the doping is usually described by an effective one-band model. This was justified by Zhang and Rice which explains that the holes create singlets hybridized from a copper atom and the four surrounding oxygens[12]. This model assumes that only one physical parameter is needed in order to describe the doping process: the number of holes per CuO_2 unit. This is also in agreement with the latter formula described in Eq. 1.1.

This description with a one relevant parameter may be oversimplified. Some researches (for example [13, 14]) have shown that the charge distribution in the different electronic orbitals affects the materials characteristics. These orbitals are the copper $3d_{x^2-y^2}$, $3d_{z^2-r^2}$ and $4s$, planar oxygen p_σ and apical oxygen p_σ and their hybridizations (see Fig. 2.6). Chmaissem *et al.* [16] claimed that the value of 0.16 holes at optimal doping is wrong, even in the BVS calculations framework.

Another point which is usually ignored is the number of holes in the parent compound. It is well accepted that there is a strong coupling between the planar copper and surrounding oxygen atoms [12] and holes create singlets by mixing copper and oxygen electronic orbitals. On the contrary, the parent compound is described as an AFM where the planar copper oxidation level is +2 (one hole in

the $3d_{x^2-y^2}$ orbital) and there are no holes in the oxygen orbitals. Simple numerical analysis shows that the copper oxidation level should be about +1.8 (0.8 holes per copper) and -1.9 for oxygen (0.1 holes) [17].

In addition to the semi-empirical BVS calculations several experimental techniques were used in order to identify the number of holes: 1. Thermopower and Hall effect [18]. 2. X-ray absorption spectroscopy [19, 20]. 3. Precise measurements of the c-axis [21]. 4. Nuclear quadrupole resonance [17].

One disadvantage common to all the above techniques is that they measure the relative number of holes and not the absolute number. In order to get absolute values it is assumed that all the materials behave as LSCO and according eq.1.1. Even in ref.[17], where absolute holes number are presented, some arbitrary choices were made in order to get the 0.16 concentration at optimal doping.

Comparison of the exact doping level of different samples of the CLBLCO compound was my first project. In the next section the unique properties of this compound are described.

1.2 CLBLCO

1.2.1 The different families

This substance has the chemical formula:

$$(Ca_xLa_{1-x})(Ba_{1.75-x}La_{0.25+x})Cu_3O_y$$

The unit cell is made of three cuboid cells [15, 16]. In the center of each cube there is a cation (similar to YBCO). The first bracket in the molecular formula defines the cation in the middle cell and the second defines the cations in the top and bottom cells. The parameter x in the molecular formula specifies the cations

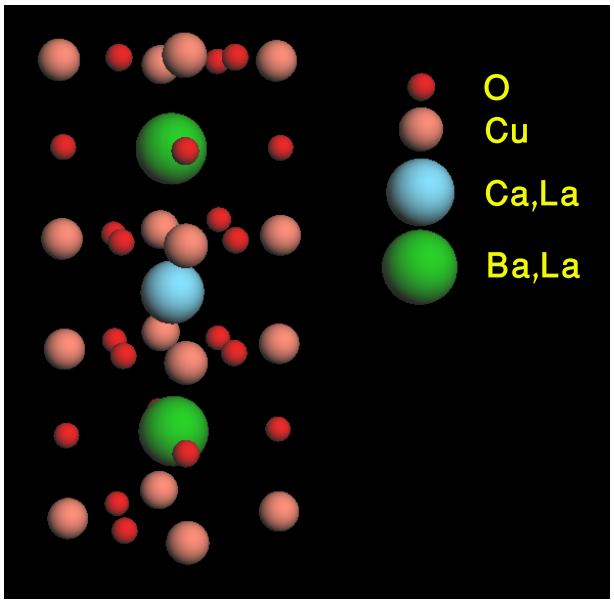

FIGURE 1.2: Unit cell of CLBLCO

make-up. In CLBLCO there are three planes of copper and oxygen- two planes of CuO_2 in both sides of the middle cell, and a third plane containing copper and oxygen in a different ratio which depends on the value of y. The oxygen density, y, varies from about 6.4 to 7.3. This oxygen density variation dopes the samples, as discussed in the previous section.

The total positive charge of the cations is constant (calcium and barium have the same oxidation level, and one can see from the molecular formula that their total amount does not change), but when x grows- the positive charge between the two CuO_2 planes decreases, and it transfers outside of the planes. We use four values of x - 0.1, 0.2, 0.3 and 0.4 (by taking different amounts of materials to make the different samples). Each value of x defines a family- for which we can create samples with a range of different y values. The physical properties of the samples depend on both variables- as we can clearly see from the phase diagram. There are systematic changes between the different CLBLCO families. The highest T_c varies as a function of x: The change in T_c^{max} is about 30% between the $x = 0.4$ family ($T_c^{max} = 81k$) and $x = 0.1$ ($T_c^{max} = 57k$). The highest Néel temperature (T_N^{max}) also increases as a function of x.

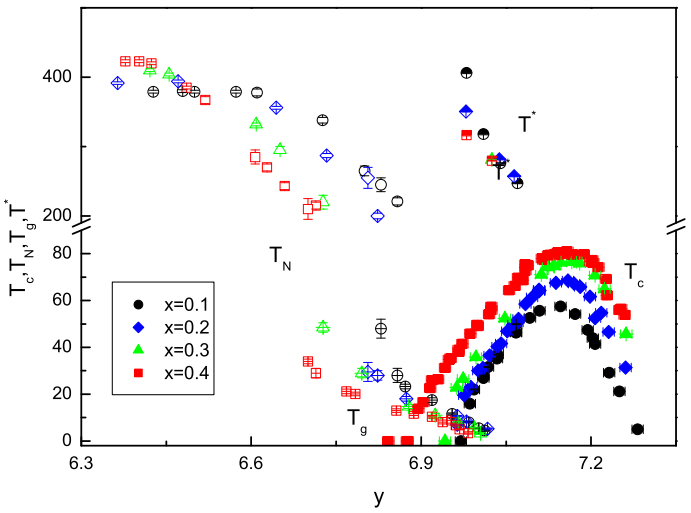

FIGURE 1.3: CLBLCO phase diagram
The four different $(Ca_xLa_{1-x})(Ba_{1.75-x}La_{0.25+x})Cu_3O_y$ families: x=0.1, 0.2, 0.3 and 0.4. T_c, T_N, T_G and T^* vs. oxygen density.

1.2.2 Scaling

Due to the systematic behavior of CLBLCO, the four different phase diagrams in Fig. 1.3 can be reduced into one unified diagram in three steps [22, 23, 24, 25, 26]: 1. Extracting the values of the in-plane AFM coupling J from T_N for each family by dividing out the interplane coupling contribution. 2. Dividing J, T_g, and T_c of each family by T_c^{max} of that family. 3. Stretching the oxygen density axis for each family around its value at T_c^{max} (y_{max}), namely, introducing the quantity $\Delta p_m = K(x)(y - y_{max})$, where $K = 0.76, 0.67, 0.54, 0.47$, for the $x = 0.1$ to 0.4 families respectively. The resulted scaled phase diagram is shown in Fig. 1.4. It is important to mention that the K's ratio between the $x = 0.4$ and $x = 0.1$ families is $1 : 1.62$, a number that will rise again in the results section.

It was speculated that the horizontal stretching in the scaling process is needed because the number of planar holes for a given oxygen density, y, is family-dependent (x-dependent). There were several attempts to find a relation between the number of holes in the CuO_2 plane and oxygen density of CLBLCO. Chmaissem *et*

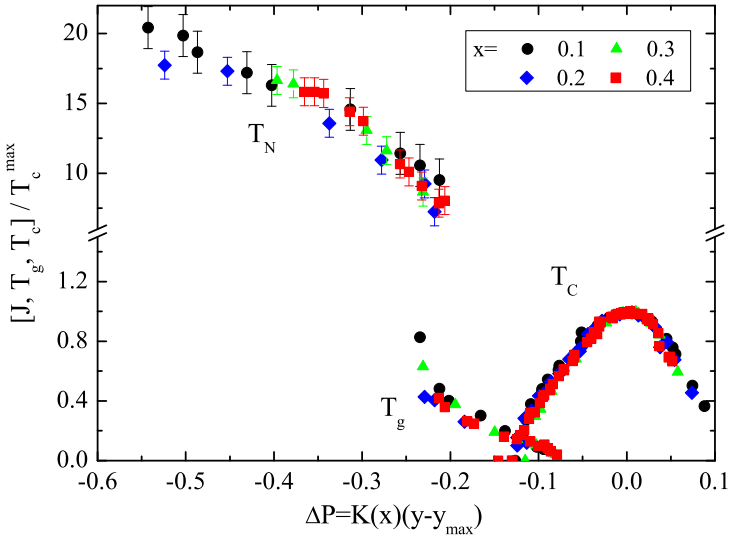

FIGURE 1.4: CLBLCO scaled phase diagram.
The scaling process is described in the text [23].

al. used BVS calculations based on structural parameters determined by neutron diffraction [16]. Keren *et al.* [27] measured the in plane ^{63}Cu NQR parameter $^{63}\nu_Q$ which is shown in Fig. 1.5, and Sanna *et al.* experimented with x-ray fine structure [19]. The conclusion of these researches was that there are two types of holes in the planes, and only the "mobile holes" participate in the SC. According to this scenario the K's values are the fraction of mobile holes of the total number of holes.

1.3 The isotope effect

The isotope effect is usually described using the isotope exponent α via the relation

$$T_q \propto M^{-\alpha_q} \tag{1.2}$$

where T_q is a phase transition temperature and M is the isotope mass. In many conventional superconductors α_c (the isotope effect on T_c) was found to be very

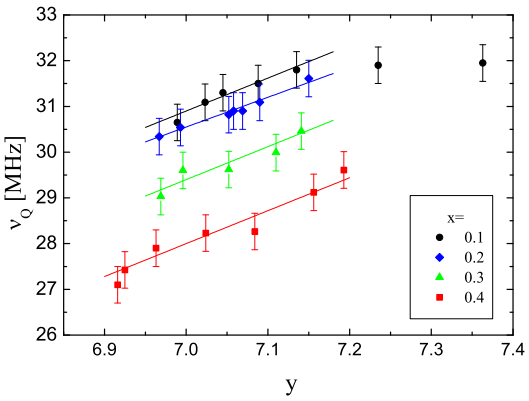

FIGURE 1.5: Copper NQR vs. oxygen density in CLBLCO
^{63}Cu NQR frequencies in CLBLCO for different values of x and y, taken from [27]. The different lines' slopes are similar, which indicates that the number of holes is family independent.

close to 0.5 [28, 29]. The explanation of this α in terms of Cooper pairs glued by phonons was one of the triumphs of the BCS theory for metallic superconductors [1].

In cuprates the isotope effect is much more complicated and α is not single valued and varies across the phase diagram. Each phase has its own α. The consensus today is that in YBCO like compounds, close to optimal doping,

$$\alpha_c^{od} = 0.018 \pm 0.005, \tag{1.3}$$

which is very small but non zero [30]. On the superconducting dome α_c gets bigger as the doping decreases [31, 32]. In the glassy state fewer data is available, but it seems that the isotope effect reverses sign and α_g becomes negative. In extremely underdoped samples, where long range antiferromagnetic (AFM) order prevails at low temperatures, data is scarce, controversial, and with relatively large error bars [30, 33]. The most recent measurements of $Y_yPr_{1-y}Ba_2Cu_3O_{7-\delta}$ are plotted in Fig 1.6. It was found that $\alpha_N = 0.02(3)$ in the parent compound [30]. There are also several theories dealing with the variation of α along the phase diagram as described below, but since α_c and α_N are within an error bar of each other one

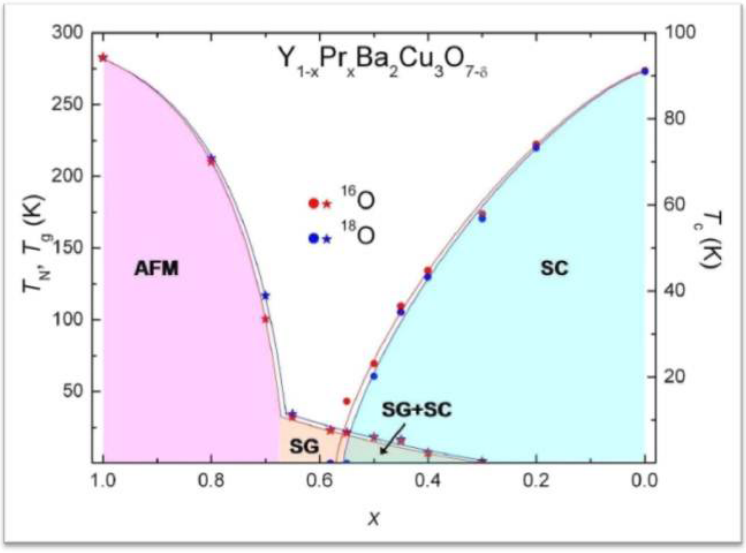

FIGURE 1.6: The oxygen isotope effect
The oxygen isotope effect on T_c, T_N and T_g in $Y_{1-x}Pr_xBa_2Cu_3O_{7-\delta}$. In the SC phase α is positive, in contrast to the AFM and SG phases. Taken from [30].

cannot contrast these theories with experiments. In particular, it is impossible to tell whether the same glue that holds the spins together holds the cooper pair together, or not. Increasing the accuracy of the IE on the Néel temperature will shed light on the role of isotope substitution.

1.3.1 Isotope effect theories

Changing the phonons frequencies: Many efforts were made to adapt the BCS scenario to cuprates, for example by adding mass-dependent term in the phonons-electrons coupling energy [35, 34]. Another theory related to a lattice movement is the creation of polarons [32].

A change in the zero-point motion: An isotope substitution may cause a change in the effective electronic Hamiltonian, as discussed by D. S. Fisher *et al.* [36], by changing the hopping term $\bar{t}$. $\bar{t}$ represents the chance of an electron hopping from a copper ion to another copper via an oxygen ion. Substituting the oxygen atom for its isotope changes, for example, the buckling angle, the vibration

frequency parallel and perpendicular to the Cu-O bond, and the Cu-Cu distance. All of these affect the hopping term. In the article above the authors estimated the change in T_c due to the change in the vibrational frequency in YBCO to be: $\alpha_c^{od} \sim 0.01$.

Affecting the doping process efficiency: The model of holes reservoir connected to the SC planes was described in section 1.1.3. Kresin and others [34, 37] have offered that the charge transfer through the apical oxygen involves a non-adiabatic process. The apical oxygen hops between two quantum states: better overlap with the planar copper or the chains copper. Changing the nucleus mass affects this hoping ratio and therefore the efficiency of hole transfer through the apical oxygen.

Affecting the superfluid density: Recent theoretical calculations show that the superfluid density can be affected by the isotope substitution purely from conservation of the total number of phonons states. This happens when there is a weak coupling between phonons and the electronic wavefunction [38]. In this model the isotope effect does not change directly the SC order parameter or the critical temperature.

Chapter 2

Experimental methods

2.1 Samples preparation

The samples are prepared by solid state reaction. Raw powders are machine milled and baked in air at 950 °C for one day and re-grounded repeatedly 3 times. Then the powder is pressed into pellets, and the pellets are sintered for 65h in flowing oxygen at 965 °C, and cooled at a rate of 10 °/h. Afterward, the samples are taken into the enrichment system, as described in the following paragraph. The different oxygen content (of the enriched samples) is achieved by reduction in a tube furnace. It is done in flowing gas (oxygen or nitrogen) environment at a chosen diffusing temperature for 48h, after which the sample is quenched. We use different diffusing temperatures in order to get different oxygen densities. This density is measured by either iodometric titration (described in [39]) or by comparing the samples T_c (measured with SQUID) to the phase diagram.

2.1.1 The enrichment system

In the oxygen isotope enrichment procedure the samples are weighed and put in a furnace, which is then evacutaed and sealed. Gas enriched with the desired

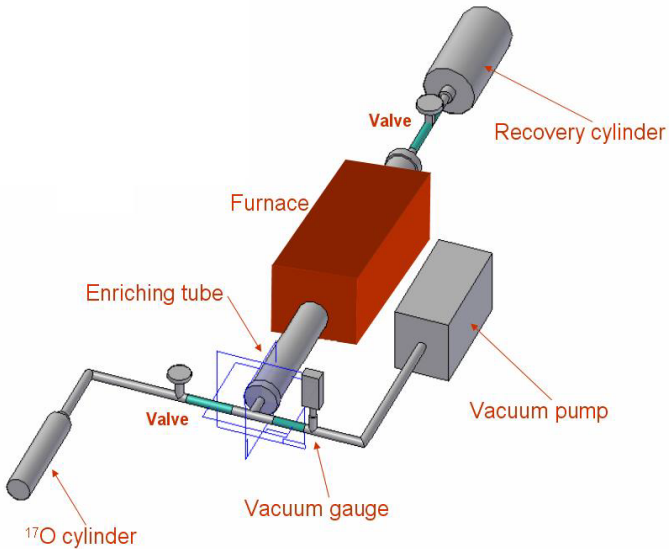

FIGURE 2.1: The enrichment system

isotope, either ^{18}O or ^{17}O, is released into the tube with the sample. The tube is sealed again, and heated to 520 °C for 5 days, cooled to 320 °C for 5 days, and then cooled to room temperature. The final isotopic fraction in the sample is equal to the initial number of isotope atoms in the gas divided by the total number of oxygen atoms (in the gas and the samples). After the enrichment process is over, some of the gas (which contains isotope) can be trapped by opening the tube to a recovery cylinder. The cylinder is put in liquid nitrogen- so its pressure is reduced and it pumps the gas. The leak rate of the system is about $20\frac{mbar}{day}$ or $0.5 \cdot 10^{-7}\frac{liter}{sec}$ (the system volume is about $1.3liter$).

The amount of isotope in the samples used for the μSR were checked after the experiments. Small piece of the sample was heated at a constant rate and the molecules desorbed were analyzed using mass spectrometer. Typical data is presented in Fig. 2.2: The green, red and blue lines represent molecular mass of 36, 32 and 34 g/mol, respectively. Those molecules are composed of O_2 with two ^{18}O atoms, two ^{16}O atoms and one atom of each isotope, respectively. The horizontal

axis shows the time from the beginning of the measurement (which can be translated into the sample temperature), the vertical axis is the ionic current intensity (which is proportional to the number of ions). From the ratio between the areas under the graphs, the isotope fraction in the sample can be calculated:

$$d_{18} = \frac{A_{36} + 0.5A_{34}}{A_{36} + A_{34} + A_{32}} \tag{2.1}$$

where A_m is the area under the graph of the molecule with molecular mass m g/mol. Before the μSR measurements the isotopic fraction of ^{18}O was about 80%, but when we measured the samples after the experiments it reduced to slightly above 70%.

2.2 Superconducting quantum interference device

The SQUID measures the change in magnetic flux in a loopinduced by a movement of a sample. The magnetic moment of the sample can be calculated from the change in the junctions current. We use SQUID to find the SC phase transition temperature: Above T_c the sample is paramagnetic, with a small magnetic moment parallel to the external magnetic field. Below T_c the sample becomes diamagnetic: the magnetic moment is bigger and antiparallel to the external magnetic field. In Fig. 2.3 the magnetic moments of four samples of the $x = 0.1$ family are shown. In the small inset their locations in the phase diagram, extracted from the measured T_c, are marked.

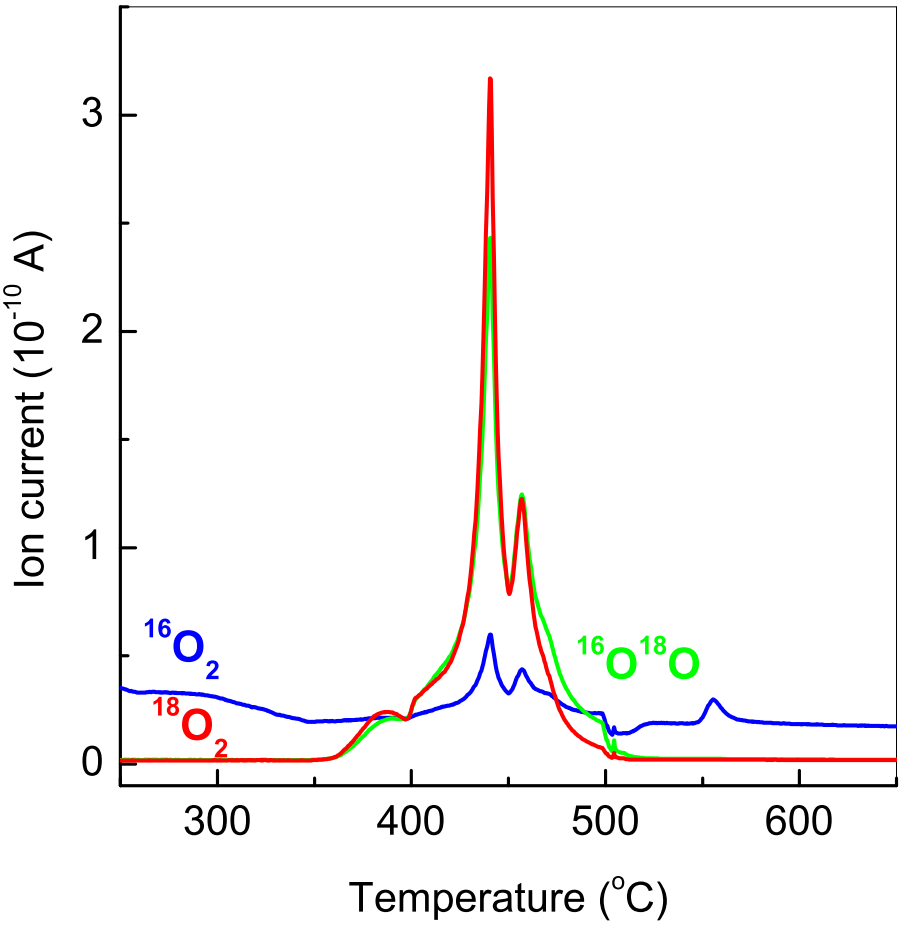

FIGURE 2.2: Verification of the isotope percentage
The deposited oxygen molecules from a samples. The green, red and blue lines represent molecular mass of 36, 32 and 34 g/mol, respectively. This graph shows that the ^{18}O isotope fraction in the samples is bigger than 70% (see text).

2.3 Nuclear magnetic resonance

2.3.1 The basic concept

NMR is a method used to measure the local electro-magnetic field at a nucleus site[40, 41, 42]. It measures the magnetic flux created by nuclei while they move from one quantum energy level to another. The Hamiltonian determining the

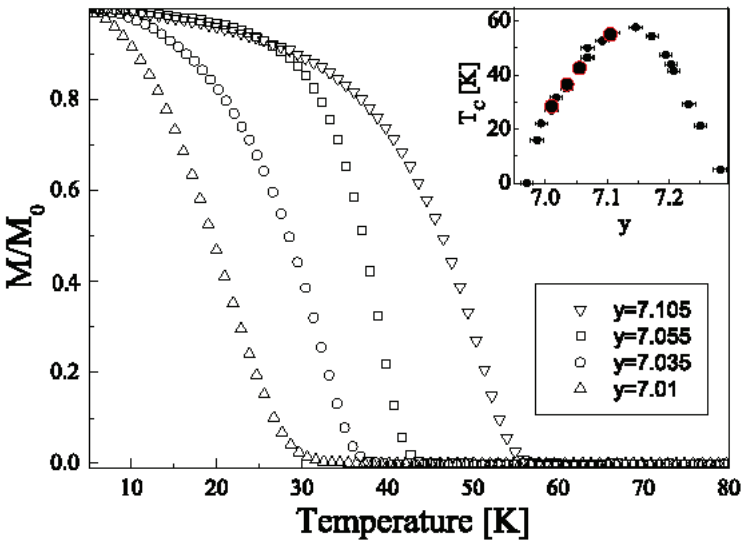

FIGURE 2.3: SQUID measurements
Magnetic moments of the SC samples of the 0.1 family at a field of -5G. At the transition temperature the magnetic moment goes to zero. The oxygen density values were obtained from the known phase diagram, as can be seen in the small inset (the four samples are marked).

energy levels (without terms irrelevant for our experiments) can be written as[43]:

$$\mathcal{H}_{NMR} = \mathcal{H}_{Zeeman} + \mathcal{H}_{Quadrupole} \tag{2.2}$$

The first term $\mathcal{H}_{Zeeman} = -\gamma I_z H_0[1 - \sigma_i]$ is the *Zeeman Hamiltonian* related to the external magnetic field H_0 into which we put the sample and γ is the nuclear gyromagnetic ratio (which is $\gamma = 5.77$ MHz/Toxygen for ^{17}O). I_z is the nuclear spin component parallel to the external magnetic field. The shift tensor, σ, is in the order of 10^{-4} or less. There are two main contributions to this tensor: The *Chemical Shift* and the *Knight Shift*.

The *Chemical Shift* is the change in the NMR frequency caused by electrons in the inner atomic shells. Electron currents in the orbitals around the nucleus are induced due to the external magnetic field and change the local magnetic field. *The Knight Shift* is created by polarization of the conducting electrons in response

to the external magnetic field. This shift is about an order of magnitude bigger than the Chemical Shift, and it is proportional to the density of states near the fermi level.

The shifts tensor can be diagonalized in its principal axes system. Using the definitions: $\sigma_i = (k_x + k_y + k_z)/3$, $\sigma_{aniso} = (k_y - k_x)/2$ and $\sigma_{ax} = (2k_z - k_x - k_y)/6$ the energy splitting between levels are:

$$\Delta E = h\gamma H_0[1 - \sigma_i - \sigma_{ax}(3cos^2(\theta) - 1) - \sigma_{aniso}sin^2(\theta)cos(2\phi)] \tag{2.3}$$

Here the angles are defined in the principle axis of the shifts tensor. In the CLBLCO system both σ_{aniso} and σ_{ax} are in the order of 10^{-6} or less and therefore negligible.

In an experiment a sample is placed in a strong magnetic field which splits the nuclear energy levels, as described in Eq. 2.3. This splitting creates magnetic moment of the nuclei parallel to the Zeeman field (assuming equilibrium and using the Boltzmann factor). In this section this moment will be described classically.

When magnetic pulse is applied in direction perpendicular to the Zeeman field, at the resonance frequency, the nuclear spin effectively feels only the varying field. This simple resonance concept is described in details in the literature (for example- [40, 41, 42]). The nuclear magnetic moment, the spin, will precess around the magnetic field direction in frequency γH_1. The applied magnetic field strength, H_1, and the pulse duration, $\frac{1}{2}t_\pi$, are chosen to fulfill the requirement $\gamma H_1 t_\pi = \pi$, and therefore after the pulse the spin will lie in the plane perpendicular to the Zeeman field direction. The spin feels magnetic field (H_0, in the z direction) and therefore it precesses at frequency ν. In conventional NMR this precession is detected by a coil: Due to Faraday law the spins precession induces electric current in the coil, which is amplified and measured. This NMR signal is basically the applied current as a function of time. Fourier transform of the data gives the

value of ν (using Eq. 2.3):

$$\nu = \gamma H_0[1 - \sigma_i] \tag{2.4}$$

The resulted NMR shift $\nu - \gamma H_0$, will be proportional to the external magnetic field. In order to compare measurements at different fields (and therefore different resonance frequencies) the results are presented as a function of ppm from a known reference. We use ppm from oxygen in water:

$$ppm = \frac{\nu_0 - \nu}{\nu_0} 10^6 \tag{2.5}$$

where $\nu_0 = \gamma H_0$ is the water resonance frequency.

The oxygen line is much broader than the frequency window that can be measured at a given magnetic field and therefore field step spin echo integral spectroscopy is used ([44] and Appendix 5.2): the frequencies are kept constant while sweeping the external magnetic field. For each field spin echo sequences are summed and then Fourier transformed. The intensity as a function of the external field $I(H)$ is the integral over the real part of the FT.

2.3.2 Relaxation of nuclei in solid

When experiment is done, the spins do not precess in vacuum and therefore the signal will decay. The first relaxation mechanism is the energy loss of the nuclei to the lattice which allow them to return to the equilibrium state (in the classical description the spins rotate back to the z direction). The parameter T_1 (or the rate $\frac{1}{T_1}$) describes the typical relaxation time. The magnetization of the sample along z will recover as

$$M_z(t) = M_z(0)[1 - e^{-\frac{t}{T_1}}] \tag{2.6}$$

The second relaxation mechanism is due to the fact that the precessing frequencies of the spins are not identical: after a typical time T_2^* the spins lose coherence.

The different frequencies are caused by different local fields, either because of intrinsic induced field distribution or non-uniform external magnetic field. The magnetization amplitude will decay at the rate $e^{-\frac{t}{T_2^*}}$.

In pulse NMR the data is an average over many sequences results, i.e: after $\pi/2$ pulse the data is collected, then another $\pi/2$ pulse is applied, the data is collected again and so on. The time that passes between the end of the data collection and the next pulse is called repetition time (t_r). In our experiments it is much longer than the data acquisition time. For accurate measurements the common repetition time is $t_r = 5T_1$ after which 99% of the magnetic moment along the z-axis recovers (from Eq. 2.6). If less accurate experiments are performed using shorter t_r, for the same time window t_{total} there are more sequences (more data is collected). Since the signal to noise ration intensity goes like the square root of the number of sequences N, the total intensity is:

$$I_{total} = \sqrt{N} \cdot I_{pulse} \propto \sqrt{\frac{t_{total}}{t_r}}[1 - e^{-\frac{t_r}{T_1}}]$$

where I_{pulse} is the intensity of a single pulse sequence and we use the magnetization recovery described in Eq. 2.6. The repetition time that maximize the intensity can be found by a simple derivation:

$$\begin{aligned} \frac{\partial I_{total}}{\partial t_r} = 0 \rightarrow \frac{\frac{1}{T_1}e^{-\frac{t_r}{T_1}} \cdot \sqrt{t_r} - \frac{1}{2}t_r^{-\frac{1}{2}}[1 - e^{-\frac{t_r}{T_1}}]}{t_r} = 0 \\ x \equiv \frac{t_r}{T_1}; \quad xe^{-x} - \frac{1}{2}[1 - e^{-x}] = 0 \quad \rightarrow \quad 2x = e^x - 1 \end{aligned} \tag{2.7}$$

Numerical solution of Eq. 2.7 yields $t_r = 1.25T_1$.

In many experiments different nuclear sites can be observed simultaneity. If T_1 of one of the sites is much shorter than the other sites, short enough t_r will reduce the signals of all other sites compared to the selected site (their spins are not recovered between sequences).

2.3.3 Hamiltonian of quadrupole nucleus

Quadrupole nucleus such as ^{17}O can be viewed as a non spherical charge distribution whose energy depends on its orientation with respect to the local electric fields. The quadrupole hamiltonian is given by

$$\mathcal{H}_{Quadrupole} = \frac{eQV_{zz}}{4I\left(2I-1\right)}\left[3I_z^2 - I^2 + \eta\left(I_x^2 - I_y^2\right)\right] \tag{2.8}$$

where $\mathbf{I}$ is the nuclear spin operator in the 5/2 representation, and eQ is the ^{17}O quadrupole moment. The second term is written in the electric field gradient system representation where the EFG tensor is diagonal, $V_{zz} = \frac{\partial^2 V}{\partial z^2}$ is the EFG largest eigenvalue, and $\eta = (V_{xx} - V_{yy})/V_{zz}$ is the EFG asymmetry. The quadrupole frequency, ν_Q, is defined as $\nu_Q = \frac{eQV_{zz}}{4I(2I-1)}$. In the limit of small quadrupole frequency compared to $\gamma\hbar H$ and using Eq. 2.8, the energy difference between two nuclear spin states $\Delta E_{m\to m-1}$ is given by [43]:

$$\Delta E_{m\to m-1} = \gamma h H[1-\sigma_i] - h\nu_Q[\frac{1}{2}(3\cos^2(\theta)-1) - \frac{1}{2}\eta\sin^2(\theta)\cos(2\phi)](m-\frac{1}{2}) \tag{2.9}$$

where m is the nuclear spin component parallel to the external (Zeeman) magnetic field, and θ and ϕ are the angles between $\mathbf{z}$ and the external magnetic field. A resonance occurs when the frequency $f_m\left(H, \nu_Q, \sigma_i, \eta, \phi, \theta\right) = \Delta E_{m\to m-1}/h$ equals the applied frequency f. In powder, all possible orientations and line broadening must be taken into account. Therefore, the spectrum is given by

$$I(H) = \sum_{m=-3/2}^{5/2} W(m) \int_0^\infty d\sigma_i' e^{-\frac{(\sigma_i'-\sigma_i)^2}{2\Delta\sigma_i^2}} \int_0^\infty d\nu_Q' e^{-\frac{(\nu_Q'-\nu_Q)^2}{2\Delta\nu_Q^2}} \cdot \int d\Omega\delta(f_m(H,\nu_Q',\sigma_i',\eta,\phi,\theta) - f) \tag{2.10}$$

The line broadenings in our experiments have typical values of $\Delta\nu_Q < 0.2\nu_Q$ and $\Delta\sigma_i \cong 0.002\sigma_i$. $W(m)$ represents the weights of the different transitions and is taken as fit parameter. All five transitions and the total NMR line defined in

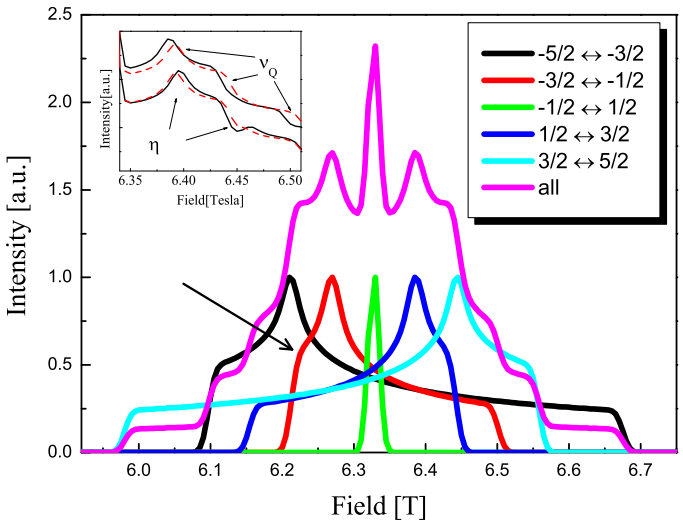

FIGURE 2.4: Theoretical NMR line
The five different transitions lines and the resulted oxygen 17 NMR line. Field sweep line at a frequency of 36.525MHz, $\nu_Q = 1$ MHz and $\eta = 0.33$. The arrow marks the transition which appears in the graphic demonstration of the fit (Fig. 2.5). In the inset: Theoretical plots of samples with different ν_Q (top lines) and different η (bottom lines), as explained in the text.

Eq. 2.10 are plotted in Fig. 2.4. The high field side of the theoretical lines for $\nu_Q = 0.95$, 1.03 MHz (with $\eta = 0.33$) and of $\eta = 0.28$,0.32 (with $\nu_Q = 1.02$ MHz) are plotted in the inset. Arrows mark the regions in which η and ν_Q changes have the most effect on the spectrum, and enable us to distinguish between these parameters. Graphic demonstration of the intensity calculation at a given field (from Eq. 2.10) is plotted in Fig. 2.5.

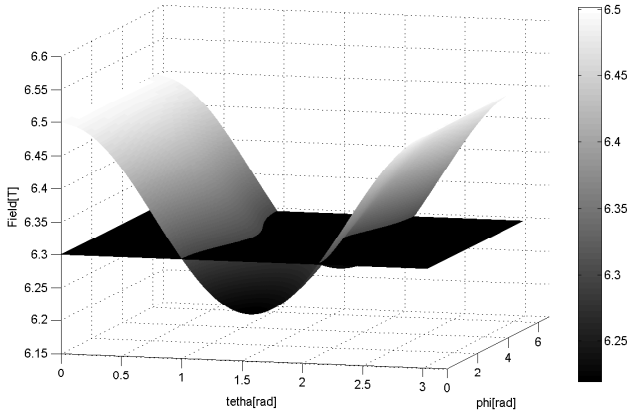

FIGURE 2.5: Graphic description of the theoretical line
The resonance fields of the second transition (which is marked in Fig. 2.4) as a function of θ and ϕ when $\nu_0 = 36.525MHz$, $\nu_Q = 0.98MHz$ and $\eta = 0.32$. There is a limited range of fields which fulfill the resonance condition. The black plane shows the $H = 6.33T$ plane. The intersection of the plane and the curve is proportional to the NMR intensity at $H = 6.33T$.

2.3.4 NQR of planar oxygen in CLBLCO

In the previous section the quadrupole frequency, ν_Q, was defined. It is proportional to the second derivative of the electric potential along the axis where its value is maximized (V_{zz}). The classical formula for V_{zz} of a nucleus is $V_{zz} = \int \rho(\overrightarrow{r})\frac{r^2-3z^2}{r^5}d^3r$ where ρ and r are the charge density and distance from the nucleus, respectively. The value of V'_{zz} induced by a different charge distribution given by $\rho'(\overrightarrow{r}) = \xi^3\rho(\xi\overrightarrow{r})$, where ξ is a constant, is

$$V'_{zz} = \xi^3 V_{zz} \tag{2.11}$$

Therefore, when two charge distributions with the same symmetry and total charge but with different typical length are compared, the quadrupole frequency should be normalized by a factor of the typical length to the third power:

$$\nu_Q r^3 \approx q \tag{2.12}$$

The electronic wavefunctions of the CuO_2 planes in CLBLCO are described in the tight-binding model. All the atomic core shells are fully occupied (hence their total spin and angular momentum is zero). The occupation of the outer electronic orbitals controls the chemical and physical properties of the planes. These electronic orbitals are the planar oxygen p_σ (either $2p_x$ or $2p_y$), apical oxygen p_z and the planar copper $3d_{x^2-y^2}$, $3d_{z^2-r^2}$ and $4s$. They are plotted in Fig 2.6.

The EFG principal axis of the planar oxygen lies along the copper-oxygen-copper axis, while the other two axes are also parallel to the unit cell vectors. There are three contributions to V_{zz}: 1) Electrons (or holes) in the planar oxygen p_σ. 2) Electrons in the planar copper orbitals. 3) The inner shells of the planar oxygen and copper atoms and their nuclei, and the surrounding cations (La, Ba and Ca). The latter contribution is not affected by the doping process (the additional holes do not occupy these orbitals). The change in the contribution of the copper

orbitals' due to doping is much smaller than the oxygen p_σ[17]. The number of holes created in both orbitals is of the same order, but the copper orbitals are much more distant (and V_{zz} goes like one over the distance to the third power, as in Eq. 2.12).

The change in V_{zz} due to the doping process is therefore proportional to the number of holes created in the planar oxygen p_σ orbital. Furthermore, comparing the number of holes in different CLBLCO families is rather simple. The p_σ has the same symmetry in all the families. The only difference may be due to the different length scale. This distance is exactly half the unit cell parameter a (planar copper-copper distance), which was measured using neutron scattering [24]. It was found that the copper-oxygen distance varies by about one percent between the families, and by 0.1% within a family (as a function of doping). Expending Eq. 2.12 using this symmetry yields:

$$\zeta\Delta(\nu_Q a^3) = \Delta n_{p_\sigma} \tag{2.13}$$

where n_{p_σ} is the hole density in the oxygen p_σ orbital, a is the unit cell parameter, ζ is a constant (family independent) and Δ stands for the change induced by the doping process. This simple relation enables a precise characterization of doping in the CLBLCO compound using minimum theoretical assumptions.

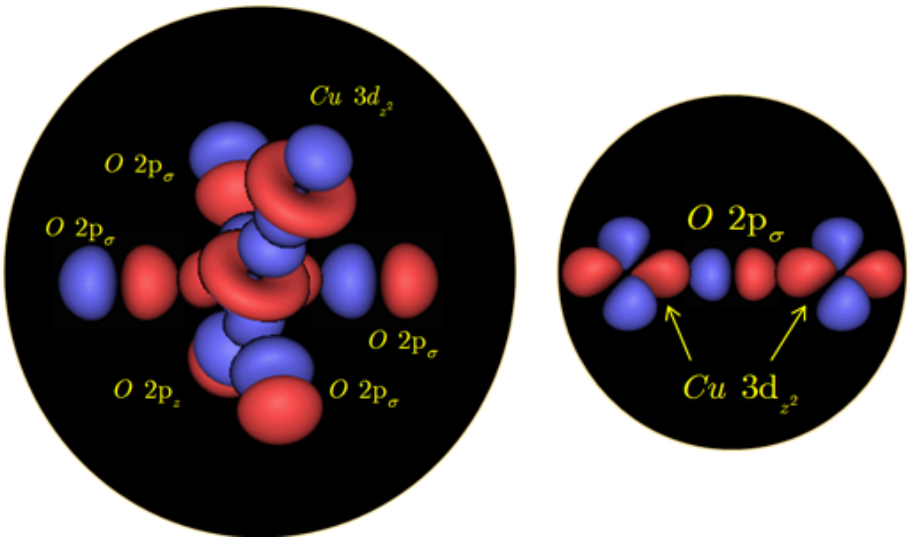

FIGURE 2.6: Planar copper and oxygen electronic orbitals
Left- planar copper. Right- Planar oxygen.

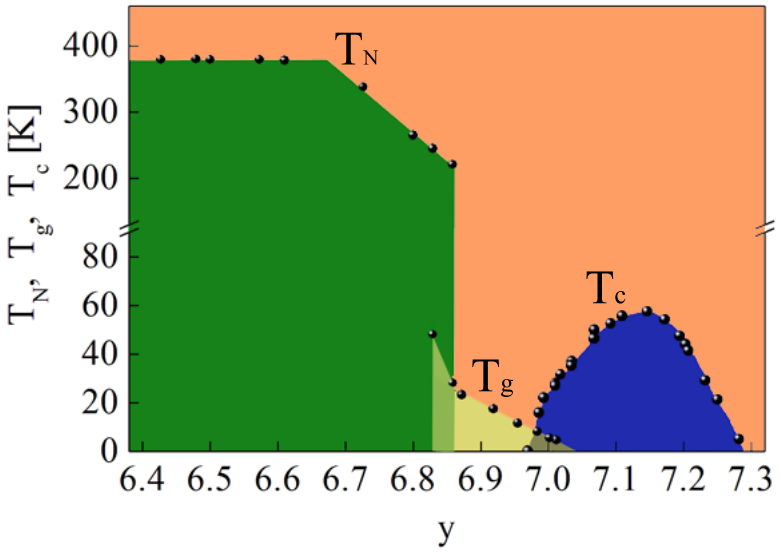

FIGURE 2.7: Phase diagram of $(Ca_{0.1}La_{0.9})(Ba_{1.65}La_{0.35})Cu_3O_y$
The critical temperatures vs. oxygen density. For low enough oxygen density the Néel temperature becomes constant.

2.4 Improving the limited oxygen isotope effect precision

The isotope effect on the critical temperatures is usually relatively small compared to the transition temperature. A major limitation on the measurements of α_N (IE of the AFM phase) is the strong dependence of T_N on doping. For example, in $Y_yPr_{1-y}Ba_2Cu_3O_{7-\delta}$, T_N decreases when the material is doped at a rate of $\Delta T_N = 2.5$ K per $\Delta y = 0.01$ (see Fig. 1.6). This strong temperature dependence is common to many other cuprates. As a consequence, it is very difficult to prepare two samples with exactly the same T_N even with the same isotope, since the smallest fluctuation in either y or δ may lead to a huge fluctuation in T_N (regardless of the isotope effect). Choosing specimens made of $(Ca_{0.1}La_{0.9})(Ba_{1.65}La_{0.35})Cu_3O_y$ overcomes this limitation. As can be seen in Fig. 1.3 for low enough oxygen density ($y < 6.6$) the Néel temperature of this compound becomes doping independent.

Another experimental limitation on the measurement accuracy is the temperature

control. The thermal contact between temperature gauge and the sample is not ideal: the temperature which is measured does not identical to that of the sample. In order the minimize this difference a flow cryostat was used. The thermal contact between the gauge and the sample was achieved not only by the contact through the sample holder but also using exchange gas which was in equilibrium with both objects.

2.5 Muon spin rotation

The muons are unstable particles which decay after a typical life time of 2.2 micro-seconds. One of the decay products is a positron, which emerges in a direction depending on the direction of the muon's spin. In a typical μSR experiment a beam of polarized muons is produced. The muons hit the sample and their spins start to rotate inside it. The rotation frequency is proportional to the magnetic field the muons feel (similar to the nuclei in NMR). Two detectors are placed in opposite sides of the sample, and the data is a histogram of the positrons hits count on each detector as a function of time. The muon spin polarization as a function of time can be estimated, and by analyzing it the local magnetic environment can be extracted.

The z component of the polarization of a muon with initial polarization in the z direction, in a static magnetic field $\mathbf{H}$, is given by the formula [45]:

$$P_z(t) = cos^2(\theta) + sin^2(\theta)cos(\gamma Ht) \tag{2.14}$$

where θ is the angle between the $\mathbf{H}$ and z and γ is the muon gyromagnetic ratio. If there is no magnetic order in the material (and without external magnetic field) each muon that hits the sample may feel a different magnetic field. If the magnetic field distribution is isotropic the angle dependence can be averaged out, and the

average muons polarization becomes:

$$P_z(t) = \frac{1}{3} + \frac{2}{3}cos(\gamma Ht) \tag{2.15}$$

When the local magnetic field is not uniform the muons will loose coherence and their average polarization will decay (similar to T_2^* in NMR). The total polarization of muons in AFM material can be described by the formula:

$$P_z(t) = P_m(ae^{-\lambda_1 t} + (1-a)e^{-\lambda_2 t}cos(\omega t)) + P_n e^{-\Delta t} \tag{2.16}$$

The relaxation rates in the fraction of the samples which is magnetic (P_m) are λ_1 and λ_2, and a is the weighting factor (which is constant and close to 2/3). The relaxation in the non-magnetic volume (P_n) is Δ. Figure 2.8 shows phase transition into the AFM phase and the fits to Eq. 2.16.

The AFM order parameter is the frequency $\omega = \gamma H$, where H is the average magnetic field at a muon site. This frequency can be easily fitted at temperatures well below the transition but is very difficult to be determined near the transition. Another approach is taking the magnetic volume fraction P_m as the order parameter, as in [24, 30]. We used a third order parameter:

$$\mathcal{OP}(T) \equiv \frac{< P_{inf} > - < P(T) >}{< P_{inf} > - < P(0) >} \tag{2.17}$$

where $< P(T) >$ is the average polarization at a temperature T, $< P_{inf} >$ is the average polarization above the transition, and the denominator normalizes $\mathcal{OP}$ to be one at zero temperature (similar order parameter was used in [46], but they used the inverse of the average asymmetry). All three order parameters are shown in Fig. 2.8(b). The transition temperatures determined using the different order parameters are in good agreement. The big advantages of the order parameter defined in Eq. 2.17 are demonstrated: it is a model free parameter which is extracted from the raw data easily with very small uncertainty, and yet gives a good

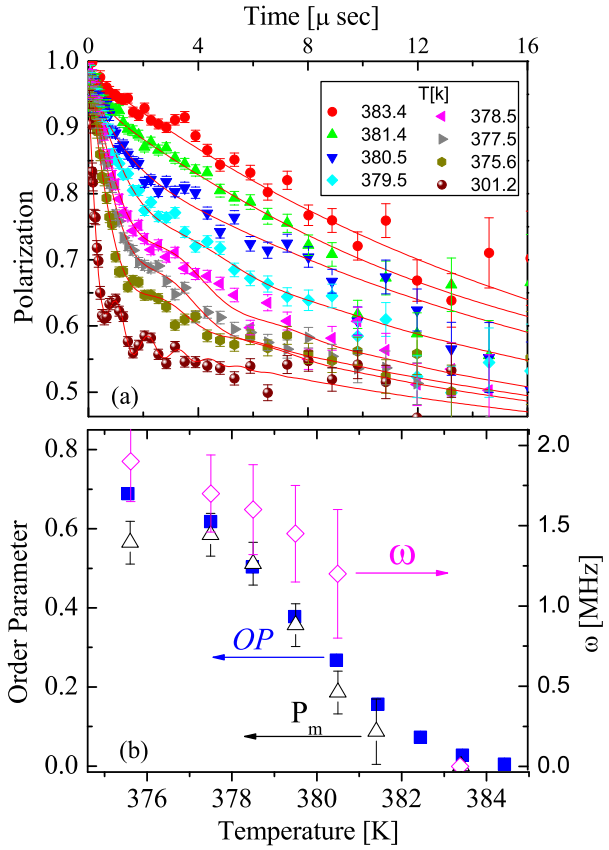

FIGURE 2.8: AFM phase transition
(a) The polarization vs. time in different temperatures. Above the AFM transition the decay rate is small, below it there is a strong decay in the polarization parameter in short times. Solid lines are fits to Eq. 2.16. (b) The order parameter defined in Eq. 2.17 (filled squares), the frequency (empty diamonds) and the magnetic fraction from Eq. 2.16 (empty triangles). The same transition as in (a).

approximation.

Chapter 3

Results and Discussion

3.1 The different oxygen sites identification

The NMR spin echo data of a CLBLCO sample is shown in Fig. 3.1. The planar and apical oxygen sites are clearly seen, and their locations are similar to those measured in YBCO [47, 48] (in the inset). The chains oxygen peak is much wider than the other peaks (and is the result of one site rather than two), and therefore it is missing. This data shows that the enrichment process is efficient and that the isotopes diffused into all possible sites.

In order to improve the signal T_1 measurements were performed. The data was fit to two decaying exponents (as explained in section 2.3.2) for the two different sites: the planar and the chain oxygen. The planar oxygen relaxation rate is much higher (T_1 is smaller), with a value of the same order as one for planar oxygen in YBCO (as shown in [47, 49]). The data is shown in Fig. 3.2 with two different fits to show the confident level in the parameters values. Ideally shorter repetition time would be used in order to further reduce the chain oxygen signal (see section 2.3.2), but due to electronics constraints the minimal repetition time we could use is 50msec.

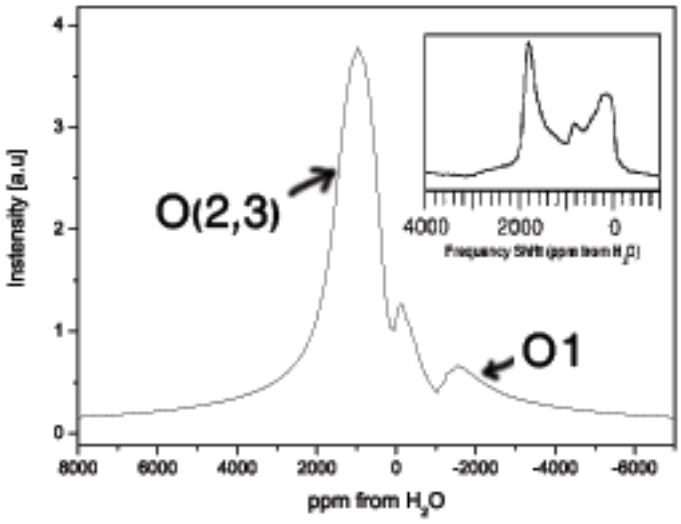

FIGURE 3.1: NMR peaks of different oxygen sites
^{17}O spin echo spectra of CLBLCO sample at 100K, 36.525MHz, 6.33T. Two of the three different oxygen sites are observed: $O_{2,3}$ is the planar oxygen and O_1 is the apical oxygen. In the inset: ^{17}O spin echo spectra of YBCO, taken at 300K, 48.8MHz, 8.45T (taken from [47]).

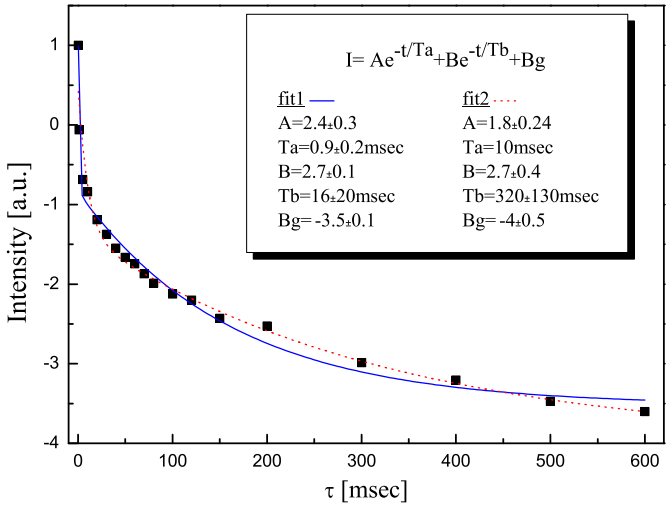

FIGURE 3.2: T_1 measurement
^{17}O spin echo spectra intensity as a function of the delay between pulses. The data was taken at temperature, frequency and field of 100K, 36.525MHz and 6.33T, respectively. The lines are fits to two exponential decays. In the solid (broken) line the faster decay time is 0.9 (10) msec.

One interesting feature of the cuprates is the pseudogap phase. Indication of this phenomenon was first obtained by NMR measurements [50]. When samples are cooled the frequency shift of the central transition changes. In most materials the temperature dependence of this shift is small but in cuprates, in the PG regime, it becomes larger [51], as can be seen in Fig. 3.3. The reason for the shift in frequency is the change in the Knight Shift upon cooling. It is related to the density of states close to the FS which changes due to the opening of the PG [52]. This shift is expected in the planar oxygen and this is an additional supporting evidence for our peak identification: the peak at lower frequency, which shifts, is associated with the planar oxygen. In Fig. 3.4 the planar peak shift for a sample with x=0.3 and y=7.08 is plotted as a function of temperature and T^* is marked. Fig. 3.5 shows the frequency of the planar oxygen peak as a function of temperature for different samples and their T^*. The extracted values of T^* are consistent with previous results using SQUID [25].

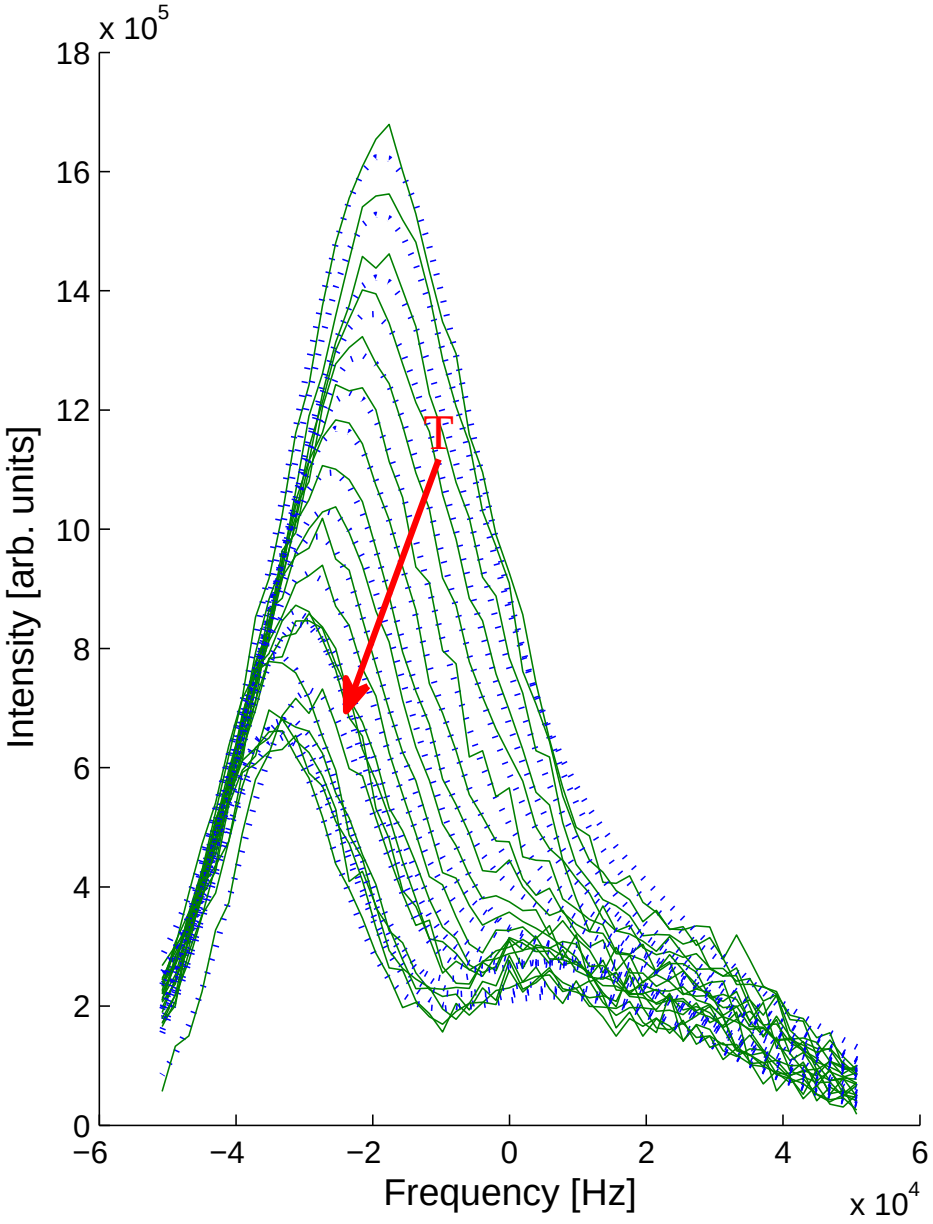

FIGURE 3.3: Temperature dependence of the NMR peaks
The data was fitted to two Lorentzians, the horizontal axis is the frequency with respect to the working frequency. The data is in solid lines, fits are in broken lines. The planar oxygen (left peak) shift is temperature dependent. The temperature range is 90K (highest peak) up to 280K. Field- 6.33T, frequency- 36.525MHz.

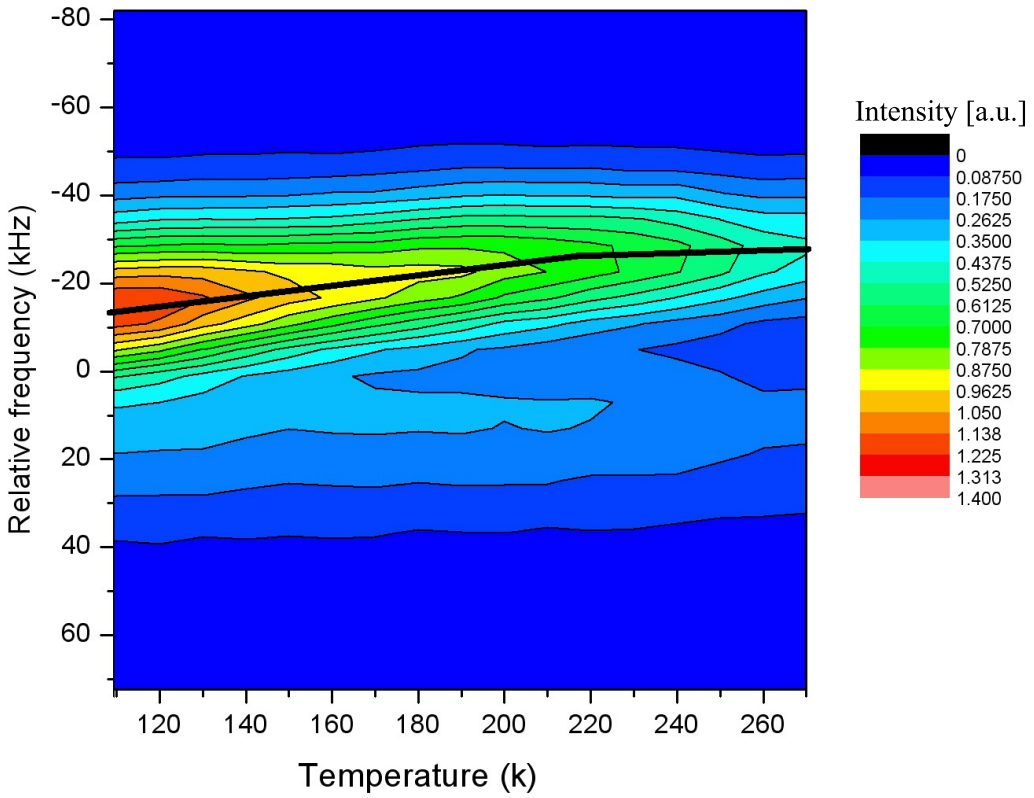

FIGURE 3.4: Temperature dependent shift of the central transition
Same data as Fig. 3.3. The solid lines are a guide for the eyes of the central peak location. This location is plotted in Fig. 3.4 as a function of temperature for different samples.

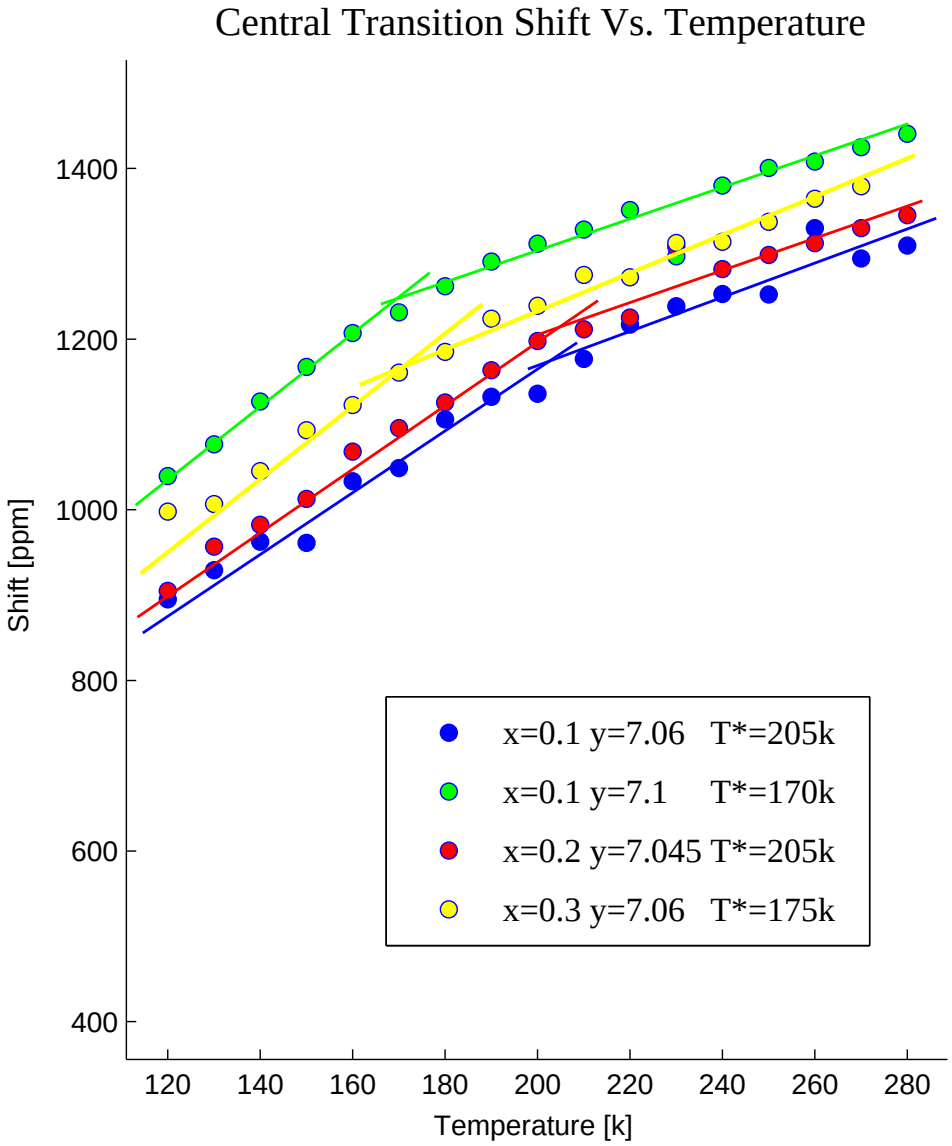

FIGURE 3.5: Planar oxygen shift vs. temperature
The change in the slope indicates a change in the density of states near the Fermi surface, related to the opening of the pseudogap.

3.2 Field sweep lines of CLBLCO

In this research the NMR lines of 11 different samples were compared. These samples belong either to the $x = 0.1$ or 0.4 families, which have a T_C^{max} difference of about 30% (about 24K). The NMR lines of three samples are presented in Fig. 3.6 : (1) $x = 0.1$ close to optimal doping, (2) $x = 0.1$ underdoped, and (3) $x = 0.4$ very under doped. Their place on the phase diagram is indicated in the small inset. There is a clear difference around 6.43 T between lines (1) and (3) but lines (2) and (3) are similar. As explained in section 2.3.4, this is a consequence of different p_σ holes densities in samples (1) and (3), and similar densities in samples (2) and (3). In the lower field regime of the underdoped sample (2) the lanthanum signal affects the spectrum. Lanthanum has a 7/2 nucleus which has a resonance at 6.1T (under our experimental conditions), which is close to the oxygen peak at 6.33T. In consequence, if the number of ^{17}O atoms in the sample is too low the low field line is dominated by the lanthanum (see also 5.3).

The dependence of the line width, or the quadrupole frequency, on the oxygen density is systematic. In Fig. 3.7 NMR lines of five samples of the $x = 0.1$ family are presented. The lines are shifted upwards so higher samples in the graph have a lower oxygen density. Two parallel lines mark shoulders locations of the lowest sample (which has the highest oxygen density). It can be seen that the shoulders locations vary with doping. The two diagonal lines are qualitative marks of the shoulders. The line width (and therefore the quadrupole frequency) grows when the oxygen density increases.

In order to quantify the differences between the samples the data was fit to the theoretical line (Eq. 2.10). NMR lines of closed to optimal doping samples with $x = 0.1$, 0.3, 0.4 and oxygen densities of $y = 7.105$, 7.07 and 7.1, respectively, are plotted in Fig. 3.8. They were found to have $\nu_Q = 1.02, 0.96$ and $0.98 MHz$, respectively. These numbers are similar to previous measurements of YBCO [47].

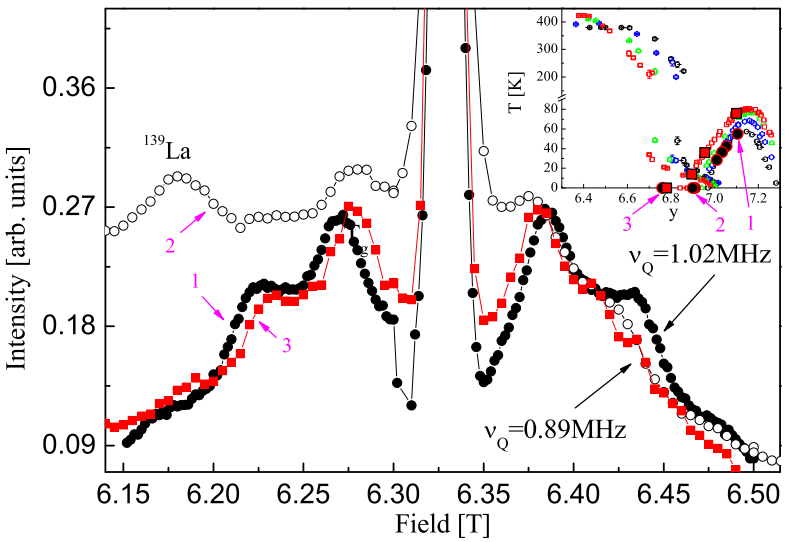

FIGURE 3.6: NMR lines of CLBLCO samples
Raw NMR data of three samples (marked in the inset): 1 (closed circles) is x=0.1 close to optimal doping (y=7.105), 2 (open circles) is x=0.1 underdoped (y=6.9), 3 (closed squares) is x=0.4 underdoped (y=6.79). From the high fields data it is clear that the quadrupole frequency of samples 2 and 3 are almost identical but different from sample 1. The dominant contribution in sample 2 at lower fields is from the ^{139}La nuclei.

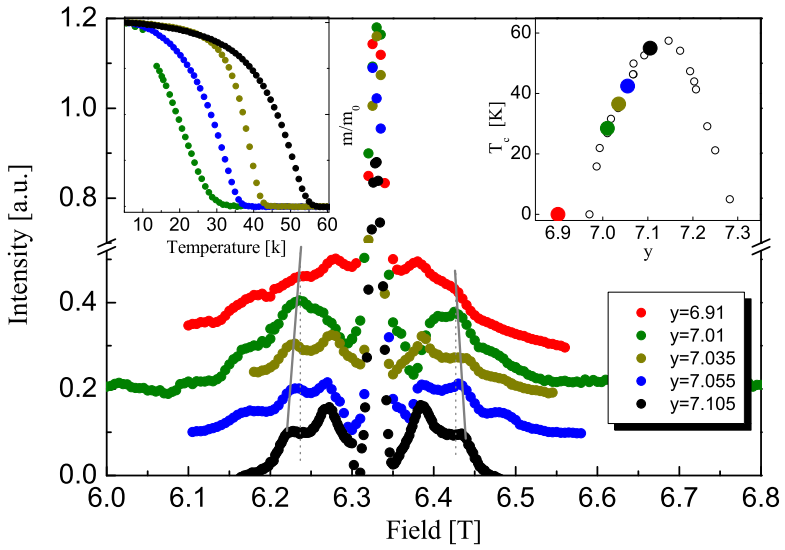

FIGURE 3.7: NMR lines of $x = 0.1$ samples
The lines are vertically shifted. The two vertical dotted lines mark the width of the top line (shoulder-shoulder width). These lines clearly do not pass through the shoulders of the other NMR lines. The solid diagonal lines, which approximately mark the widths of all NMR line, are not parallel which indicates that the widths are different. In the left panel: susceptibility measurements of the samples (T_c identification). In the right panel: the samples on the phase diagram.

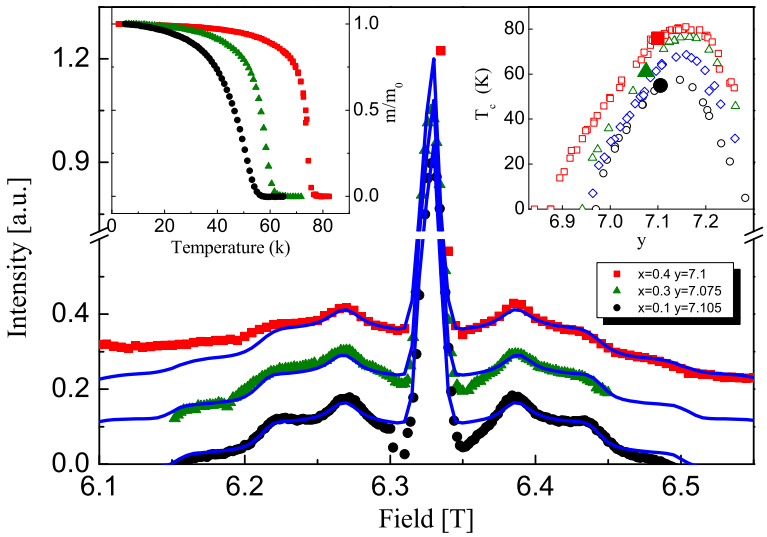

FIGURE 3.8: NMR- fitting the data
Data of closed to optimally doped samples of different families ($x = 0.1$, 0.3 and 0.4 in black circles, green triangle and red squares, respectively) at 110K, 36.525MHz. The NMR lines are vertically shifted. The blue lines are fits to Eq. 2.10. In the left panel: susceptibility measurements of the samples (T_c identification). In the right panel: the samples on the phase diagram.

3.3 Translating the oxygen density into number of holes

In Fig. 3.9 $\nu_Q a^3$ as a function oxygen densities of the two families with $x = 0.1$ and 0.4 are plotted (Samples 1, 2 and 3 are the same as in Fig. 3.6). The locations of the samples on the phase diagram are marked in Fig. 3.10. According to Eq. 2.13 the quantity $\nu_Q a^3$ is proportional to n_{p_σ} (the number of planar oxygen p_σ holes density). It can be clearly seen that the dependent of n_{p_σ} on the oxygen density varies between the two families. The data from the different families generate two different linear curves. Two straight lines are fitted to these datasets with the constraint that the slopes ratio is $1 : 1.62$, which, as mentioned in subsection 1.2.2, is the ratio of $K(0.4)$ to $K(0.1)$ (the abscissa axis stretching ratio). The measured n_{p_σ} versus y can be explained well by the two lines.

In order to get an expression for the p_σ hole doping in CLBLCO another feature of this compound was used. For each family there is an oxygen density which marks a transition between a constant T_N and a decreasing T_N as a function of y, as demonstrated in Fig. 3.10. We denote this density y_N; for the $x = 0.1, 0.2, 0.3, 0.4$ families $y_N = 6.69, 6.63, 6.52, 6.43$, respectively. Below y_N the number of the planar holes is constant (and therefore T_N is constant). Following Ref. [17], $n_{p_\sigma}(y < y_N) = 0.11$.

Another selection which was made is choosing a different set of $K(x)$: $K = 0.113, 0.098, 0.079, 0.069$, for the $x = 0.1$ to 0.4 families respectively. The ratios of the K's values of the different families remain the same as in the previous set (described in subsection 1.2.2). With these selections $n_{p_\sigma} = 0.16$ at optimal doping. The new phase diagram (critical temperatures vs. holes concentration) is presented in Fig. 3.11. Negative values of Δn_{p_σ} represent CuO_2 planes which are not doped ($y < y_N$). We would like to emphasize again that we can only quantify

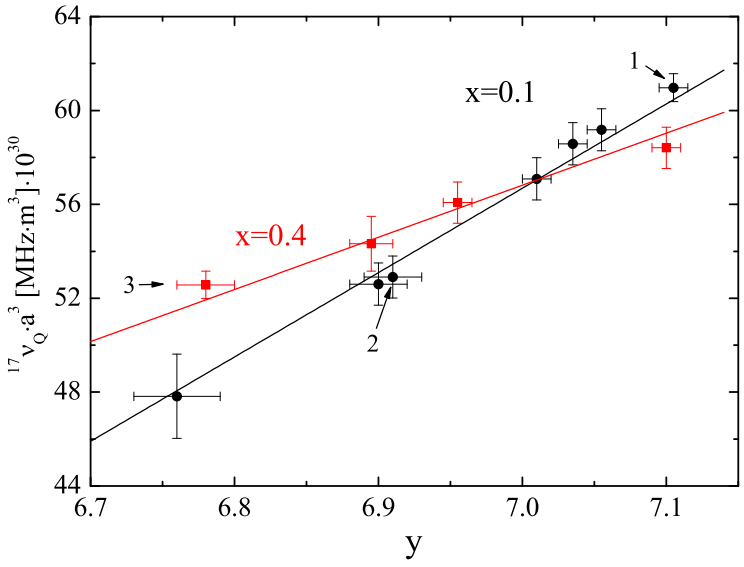

FIGURE 3.9: The number of holes vs. oxygen density
The translation of the number of oxygen atoms per unit cell (abscissa) into the number of p_σ holes (ordinate), as extracted from the NMR data. The NMR lines of samples 1,2 and 3 are shown in Fig. 3.6. The x=0.1 family is in black circles, and the x=0.4 family is in red squares. The ratio between the slopes is equal to the stretching ratio between the families in the scaling process shown in Fig. 1.3 (see text)

the doping efficiency ratio between the two different families (K's ratio), but not their absolute value.

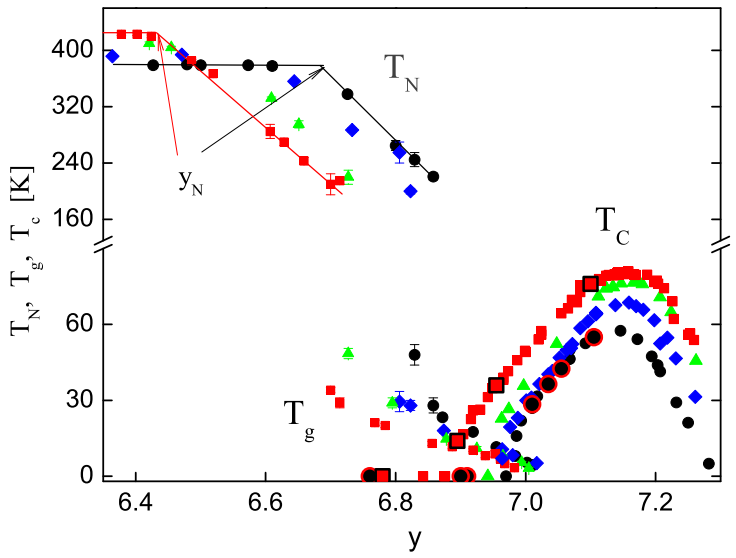

FIGURE 3.10: Identifying y_N
The oxygen density below which T_N is constant is called y_N. The y_N of the different families are identified. The location on the phase diagram of the samples which were used for this project are marked.

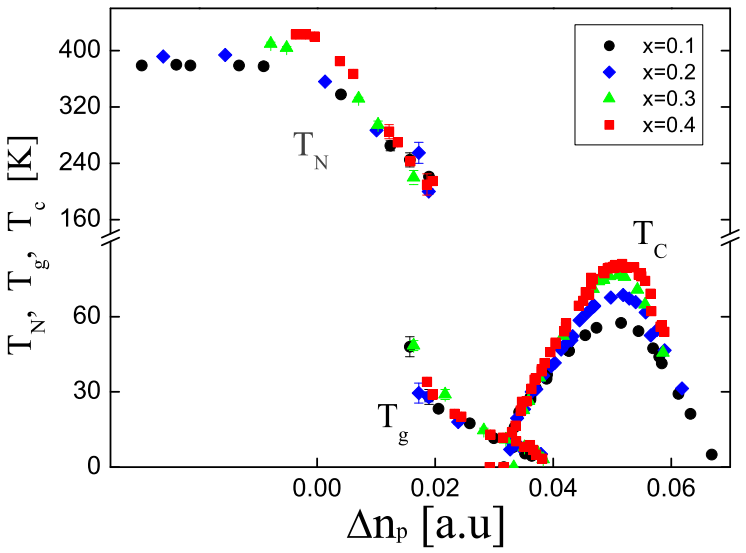

FIGURE 3.11: The new CLBLCO phase diagram
Critical temperatures versus planar oxygen p_σ holes of the different CLBLCO families.

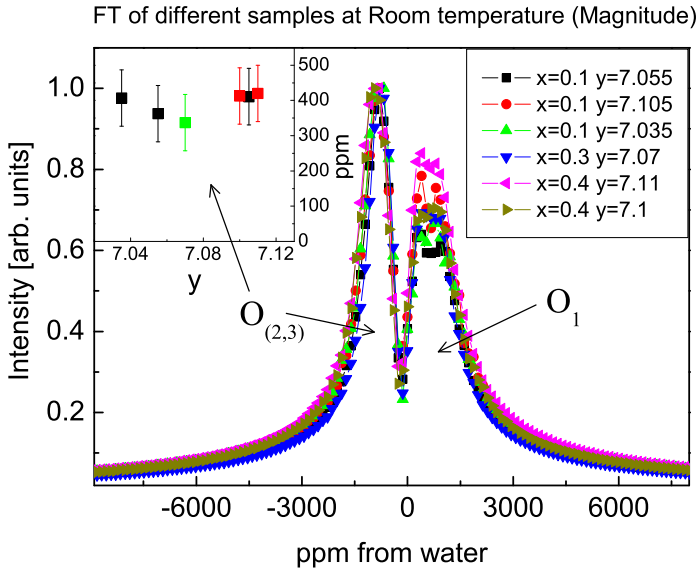

FIGURE 3.12: Room temperature NMR lines of different CLBLCO samples
In the inset: the planar oxygen widths of the different samples vs their family. There is no indication of family dependence.

3.4 The role of inhomogeneities in CLBLCO

Another point worth mentioning is the lack of evidence for different levels of impurities in the different families. The spin-echo signal of seven samples, of three different families, is presented in Fig. 3.12. The data was taken at room temperature, magnetic field of 6.33T and frequency of 36.525MHz. The planar oxygen peaks widths (as identified in Fig. 3.1) is plotted in the small inset as a function of the oxygen density. The NMR measurement is sensitive to inhomogeneities which is expressed in broadening of the peaks. The peaks widths seem to be family independent, in the experimental resolution.

The quadrupole nucleus ^{17}O enables a more direct examination of the charge distribution homogeneity. One of the parameters in the fit function (Eq. 2.10) is the width of the quadrupole frequency distribution $\Delta\nu_Q$, which is directly related to the homogeneity of the charge distributions around the different nuclei. Unfortunately, it is difficult to separate this line broadening and the broadening due to

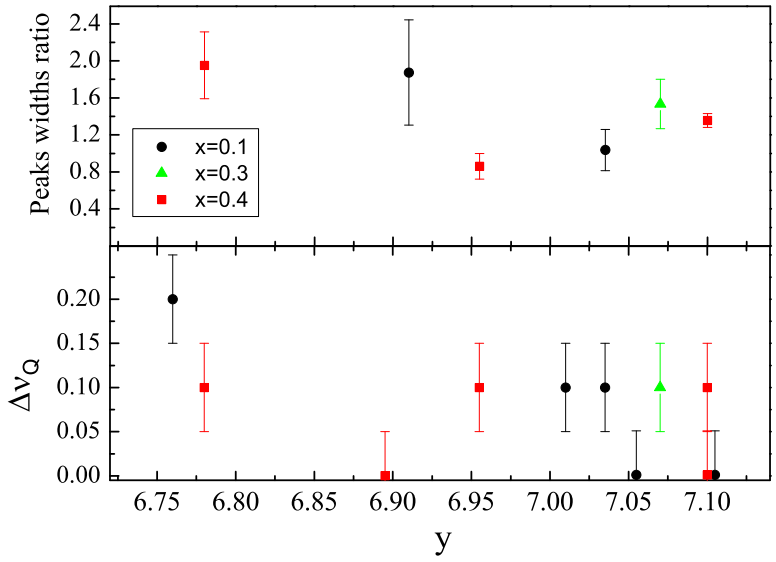

FIGURE 3.13: Line broadening of different samples due to inhomogeneities Bottom panel: the NQR frequency distribution widths ($\Delta\nu_Q$) of different samples as defined in Eq. 2.10. Top panel: the widths ratio of the peak at 6.38T and the central transition, an indication to the broadening caused by non-uniform charge distribution (see text). The sampels homogeneities are family independent.

non-unify magnetic environments (the parameter $\Delta\sigma_i$) and therefore these values have large error bars. The plot of $\Delta\nu_Q$ versus y is presented in Fig. 3.13. In order to overcome this problem another analysis was performed. In the limit of small quadrupole frequency (compared to γH) the central transition is not affected by the quadrupolar broadening (as can be seen in Eq. 2.9). In contrary, the width of the peak in fields of about 6.38T (the "η peak", see Fig. 5.5) is affected by $\Delta\nu_Q$ and $\Delta\sigma_i$. Both peaks were fitted to Gaussian and the width ratios (the η peak over the central transition widths) of different samples are presented in Fig. 3.13. The effectiveness of this analysis is limited due to the attenuation of the central peak intensity, which may affect the η peak width. A possible explanation for this attenuation is discussed in appendix 5.1. Both methods of analysis did not give conclusive results, but different homogeneities levels for different families were not observed.

3.5 The oxygen isotope effect

In this experiment the polarization of the $(Ca_{0.1}La_{0.9})(Ba_{1.65}La_{0.35})Cu_3O_y$ were measured using μSR in ISIS, RAL. The oxygen density of the samples y, was 6.55 ± 0.01, and the isotopic fraction of the ^{18}O samples was bigger than 70%. The measurements were performed across wide temperature range of 50 to 410 K. Some of the raw data of different isotopes is presented in Fig 3.14. The values of $\mathcal{OP}$ (defined in Eq. 2.17) are shown in Fig. 3.15. We determine T_N by fitting a straight line to the data in the temperature range 378 to 382 K, for each sample, and taking the crossing with the temperature axis. We find that T_N^{18}=382.49(0.34) K and T_N^{16}=382.64(0.29) K. When taking into account the isotopic fraction in the samples we obtain (using Eq. 1.2):

$$\alpha_N = 0.005 \pm 0.011. \tag{3.1}$$

Which implies that there is no oxygen isotope effect on the Néel temperature.

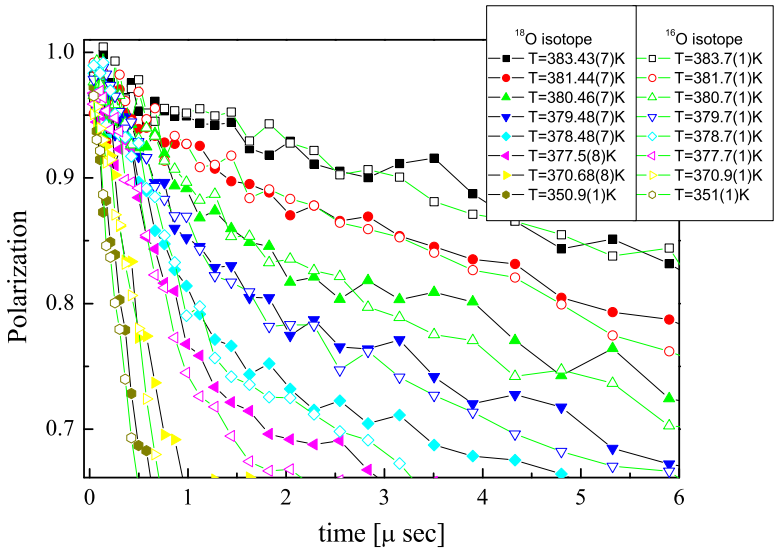

FIGURE 3.14: Raw data of the AFM phase transitions of the isotopes
The polarization vs. time at different temperatures of samples with the same y but with different isotopes: ^{18}O in filled symbols, ^{16}O in empty symbols. The temperature dependence looks identical.

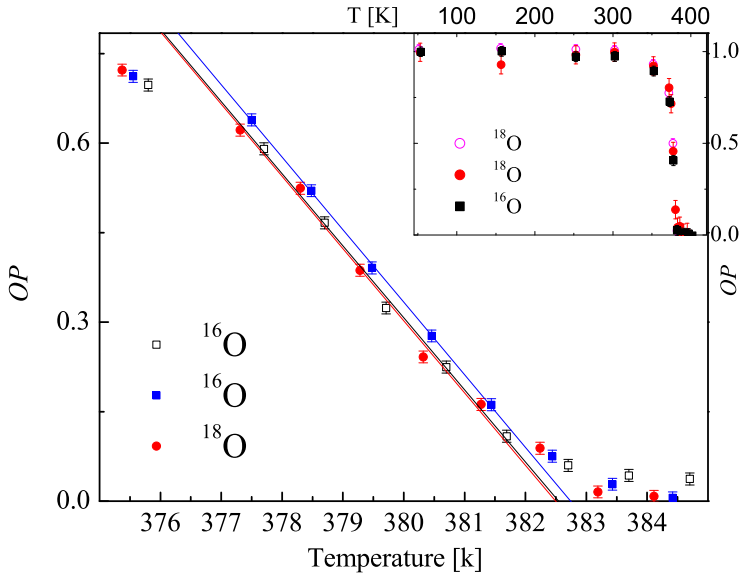

FIGURE 3.15: The OIE on T_N
The order parameter defined in Eq. 2.17 vs. temperature of samples with the same y with different isotopes. The ^{16}O samples in squares, the ^{18}O samples in circles. In the inset: the entire temperature range. The temperature dependence looks identical.

Chapter 4

Conclusions

4.1 Cuprates phase diagram

The main achievement of this work is the measurement of the number of planar holes in different CLBLCO families. We use the oxygen quadrupole frequency which is proportional to the number of holes in the planar oxygen p_σ orbital. We show that the doping efficiency is family dependent, and its ratio equals to the stretching ratio previous found (the parameter $K(x)$). This implies that this stretching is the translation from the oxygen density into the physical parameter: the planar oxygen p_σ holes density. This finding is different than previous works. BVS (used in [16]) has some theoretical arbitrariness and is not completely reliable. $^{63}\nu_Q(y)$ (used in [27]) shows no family dependence because $^{63}\nu_Q$ is sensitive to charge on the apical O_4 p_σ, Cu $3d_{x^2-y^2}$, $3d_{z^2-r^2}$ and $4s$, and $O_{2,3}$ p_σ holes simultaneously (as can be seen in Fig. 2.6) [17]; hence it is not an ideal probe and a difference in the slopes of $^{63}\nu_Q(x,y)$ could not be detected within the experimental error bars. Finally, the XFS measurements (in [19]) were performed on nearly optimally doped samples, where the difference between the number of holes between families is very small. Therefore, none of the three attempts could find a difference in the doping efficiency of the planes within experimental resolution. The oxygen

NQR has the advantage of measuring directly the dependence of oxygen p_σ hole density $n_{p\sigma}$, on the oxygen level y, and, indeed, this probe detects variations in doping efficiency.

This study of the CLBLCO compound shows that an effective one-band model is sufficient to describe the essential physics of the doping process. The physical parameter in the model is the planar oxygen $2p_\sigma$ holes density. This density defines all the phase transitions at zero temperature, regardless the superconductivity energy scale (or scales) which defines the phase transitions upon heating. This phase diagram is drawn in Fig. 4.2. Eventhough this is a general conclusion it is more difficult to be observed when two different SC are compared. When there are too many chemical differences between materials other structural effects change the phase diagram, and the isolation of the contributions related to the SC mechanism becomes very difficult. The CLBLCO compound seems to provide the solution to this problem: how to change the SC energy scale without changing other parameters.

When looking at the CLBLCO phase diagrams (Fig. 3.11) it can be speculated that the main reason for the difference is impurities. Our measurement contradicts this claim. Moreover, the finding that the same amount of planar holes is needed to change the nature of the ground state in all the families is another evidence for the minor effects of different crystal ordering on the physical properties of the samples.

The four different CLBLCO families phase diagrams can be reduced into one uniform phase diagram without using any adjustable parameter. We start with the phase diagram presented in Fig. 3.11, replace T_N with J, and divide J, T_c and T_g by T_c^{max} of each family [23, 22]. From the scaling we get a simple relation between the maximum T_c and the AFM coupling in the underdoped regime: $T_c^{max} = \xi J$, where ξ is constant (family independent). This shows that the SC energy scale is

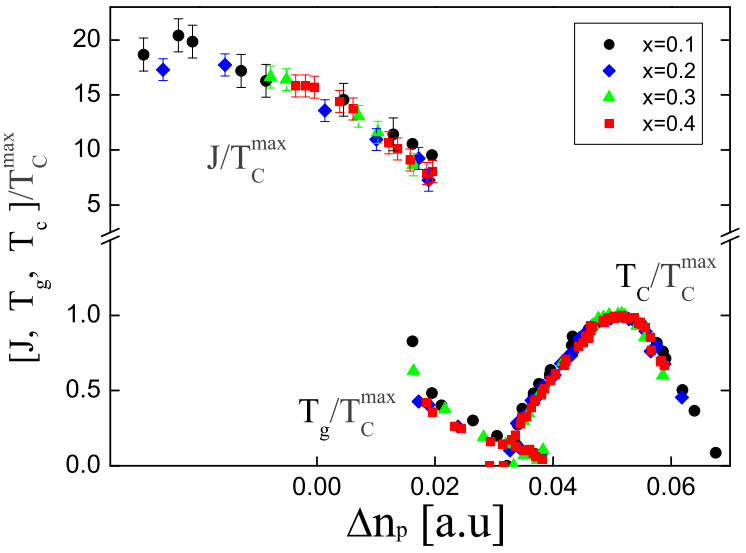

FIGURE 4.1: CLBLCO scaled phase diagram
T_C, T_g and T_N over T_C^{max} of each family versus the change in the number of planar holes. In this graph all the critical doping levels of the different families fall on the same points.

the same as the AFM energy scale of the parent compound, and therefore the SC pairing mechanism is related to magnetism.

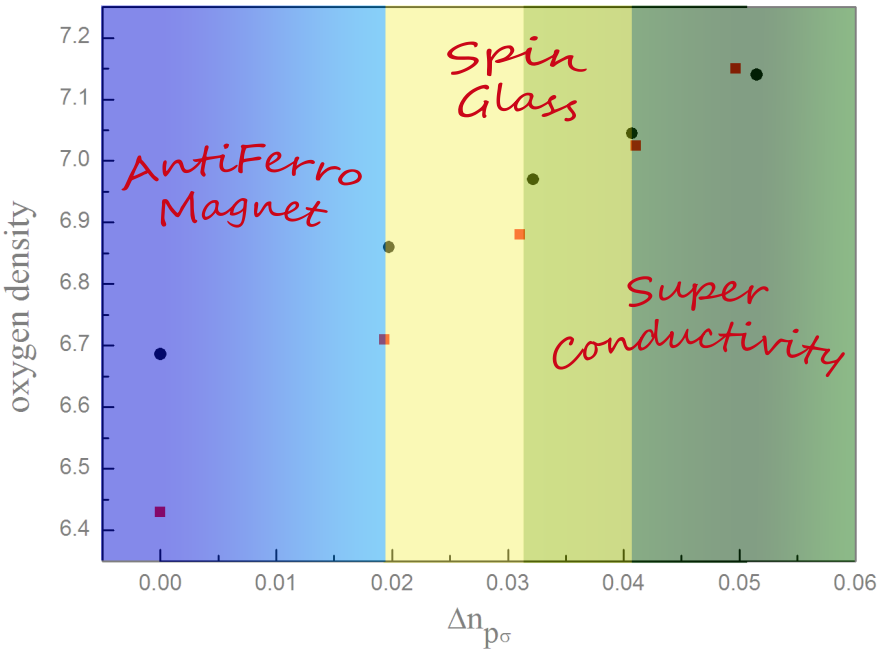

FIGURE 4.2: Generic phase diagram
The critical oxygen densities versus $2p_\sigma$ holes for the x=0.1 (black circles) and x=0.4 (red squares) families. The different phases as a function of the number of holes are marked. The universal critical doping levels can be easily seen.

4.2 Oxygen isotope effect in cuprates

We think that the finding that there is no isotope effect when the critical temperature is doping-independent is crucial. In the previous section we demonstrated that relatively small changes in the unit cell affect the holes density in the CuO_2 planes [53]. In order to examine small changes in the phase diagram it should be plotted as a function of the holes density (the physical parameter) and not parameter from the unit cell (such as y and δ from $Y_yPr_{1-y}Ba_2Cu_3O_{7-\delta}$ in Fig. 1.6). If the isotope substitution changes the holes density the effect is a horizontal shift of the critical temperatures rather than vertical shift: the critical temperature for a given number of holes does not change. Demonstration of this horizontal shift is plotted in Fig. 4.3(a) (for T_N) and 4.3(b) (for T_c): The horizontal axis is multiplied by the doping efficiency. It can be seen that a difference of about 3% in the planar holes density explains the experimental results. This argument supports the theoretical model proposed in [34, 37]. They showed that non-adiabatic charge transfer to the CuO_2 planes through the apical oxygen is sensitive to its mass: When the apical oxygen mass increases the holes concentration in the planes reduces.

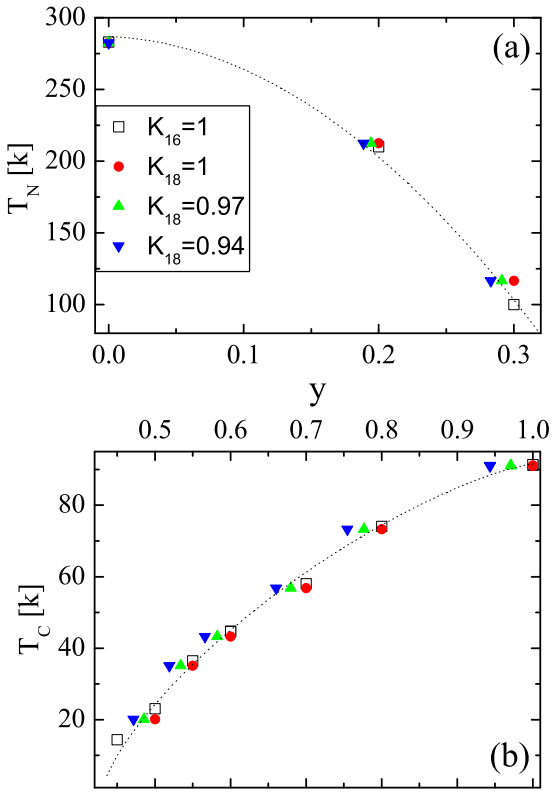

FIGURE 4.3: Oxygen isotope effect in $Y_yPr_{1-y}Ba_2Cu_3O_{7-\delta}$
Data taken from Ref. [30]. Figure (a) and (b) are demonstration of the IE using charge carriers density $p = K_i y$, instead of oxygen content y. The effect on T_N and T_c are plotted in figures (a) and (b), respectively. The values of K_i are given in the the figures. Green triangles ($K_i = 0.97$) represent reduction of 0.03% in the number of charge carriers in the ^{18}O samples compared to the ^{16}O sample. In this case both T_N and T_c are functions of p regardless of the isotope.

Chapter 5

Appendix

5.1 The effect of non-ideal pulse on the spectrum

In some of the NMR field sweep experiments the intensity was attenuated in both sides of the central transition. We speculated that the exact value of t_π (defined in section 2.3.2) may cause this deep. In order to test this hypothesis the NMR spectrum is investigated using density matrix formalism. The expectation value of a parameter m as a function of time can be found using the formula:

$$< m(t) >= Tr[\rho(t)m(0)] \tag{5.1}$$

where $\rho(t)$ is the density matrix at time t [42]. The time evolution of the density matrix (when the Hamiltonian $\mathcal{H}$ is constant) can be written as:

$$\rho\,(t) = e^{-i\mathcal{H}t}\rho_0 e^{i\mathcal{H}t} \tag{5.2}$$

This formalism can be used to describe the pulse NMR intensity. The initial spin density matrix is proportional to I_z due to the Zeeman splitting ($\overrightarrow{H_0} = H_0\hat{z}$), and therefore $\rho_0 \propto I_z$. The measured quanta in this experiment is $I_+ = I_x + iI_y$ in the rotating reference frame (which rotates around the z axis at the resonance

frequency ν). In the following sections the intensity of I_+ at the end of the pulse is calculated:

$$\left\langle I_+^{rrf}(t)\right\rangle = tr\left(\rho(t)\, I_+^{rrf}\right) \tag{5.3}$$

The free induction decay is the simplest NMR sequence: Magnetic pulse in the x direction of the rrf (in the framework of the lab the pulse is in the x direction in frequency of $\nu = \gamma H_0$) and intensity H_1 is applied for duration of $\frac{1}{2}t_\pi$, and then the signal is measured. Ideally, the pulse duration satisfies the relation $\gamma H_1 t_\pi = \pi$, and it rotates the spins from the initial z direction into the xy plane ($\frac{1}{2}\pi$ half rotation), as can be seen in the inset of Fig. 5.1(a). The sequence intensity:

$$\rho(t) = e^{-i\frac{1}{2}t_\pi\gamma\mathcal{H}_{RF}}\rho_0 e^{i\frac{1}{2}t_\pi\gamma\mathcal{H}_{RF}} \tag{5.4}$$

here the Hamiltonians are given by:

$$\begin{aligned}
\mathcal{H}_Z &= -\gamma\hbar(1-\sigma_{iso})(H_0 - \tfrac{\omega}{\gamma})I_z \\
\mathcal{H}_q &= \tfrac{1}{3}\nu_q\left(3S_z^2 - I^2 + \eta\left(S_x^2 - S_y^2\right)\right) \\
\mathcal{H}_{tot} &= \mathcal{H}_Z + \mathcal{H}_q \\
\mathcal{H}_{RF} &= \mathcal{H}_{tot} + \gamma\hbar H_1 I_x
\end{aligned}$$

Where I_α are the nuclear spin I components in the rrf. The NQR hamiltonian is diagonal in different reference frame and therefore its spin operators are marked with S. For small quadrupole frequency $\nu_q/\nu << 1$ the NQR Hamiltonian can be written in the rrf using two Euler angles:

$$\mathcal{H}_q = \nu_q(3I_z^2 - I^2)(3cos^2(\theta) - 1 + \eta cos(2\phi)sin^2(\theta))$$

Note that the rigoristic frames transformations is to write a unified Zeeman and NQR Hamiltonian and then transform it into the rrf, but it gives the same result.

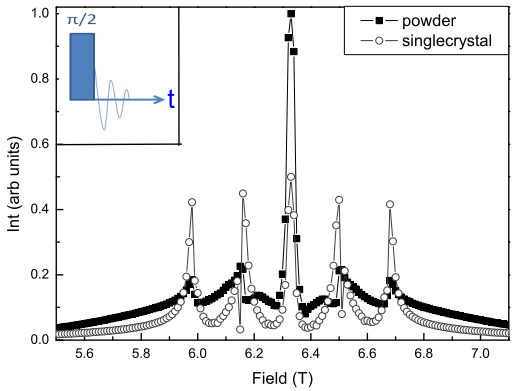

FIGURE 5.1: Field sweep spectrum of FID sequence
Numerical calculation of ^{17}O NMR spectrum using Eq. 5.4. The parameters are: $\nu = 36.525MHz$, $\nu_q = 1MHz$, $\eta = 0.32$ and ideal t_π. The powder and single crystal symbols are squares and circles, respectively. In the inset: Schematic draw of FID sequence.

In Fig. 5.2 the spectrum is plotted for different t_π values. These numerical calculations shows that the pulse duration may indeed affect the dips around the central transition.

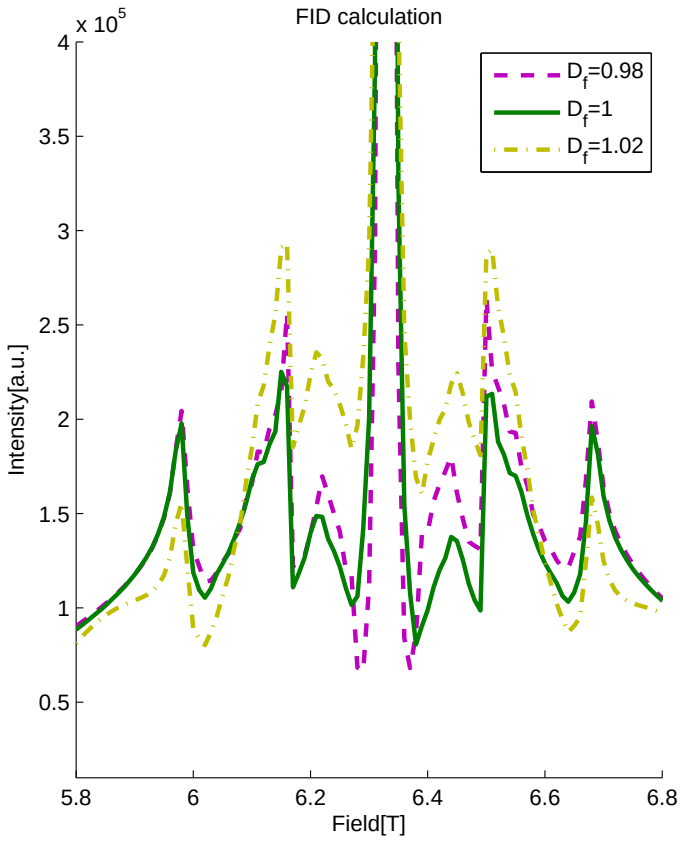

FIGURE 5.2: FID spectrum for different pulses lengths
Numerical calculation of ^{17}O NMR spectrum using Eq. 5.4. The parameters are: $\nu = 36.525MHz$, $\nu_q = 1MHz$, and $\eta = 0.32$. $t_\pi = D_f \cdot \frac{0}{\pi}$, $D_f = 0.98, 1, 1.02$ in broken, solid and broken-dotted lines, respectively.

5.2 Frequency step and sum method

Most of the NMR machines are designed to operate at narrow band width and high resolution (around 0.1ppm). In order to study very broad lines Clark *et al.* have shown that data of different frequencies (or fields) can be summed into a single NMR line [44]. They showed that by shifting each Fourier transform of a given field by a different frequency the correct NMR line is obtained (under some experimental conditions). This frequency equals to $\bar{\gamma}\Delta B_n$, where ΔB_n is the difference between the field and a chosen reference field (which is usually the resonance field of the central transition). The resulted NMR line at a given frequency is the summation of all the contributions of the different fields spectrums:

$$S(f) = \sum_{n,k} S_n(f) = \sum_{n,k} S_n(f_k)\delta(\bar{\gamma}\Delta B_n + f_k - f) \tag{5.5}$$

where $S_n(f)$ is the contribution of the n'th field for the frequency f, which can be written explicitly as the intensity of the frequency f_k of the n'th with respect to $\bar{\gamma}\Delta B_n$. Here $\bar{\gamma}\Delta B_n$ is the frequency offset of the field.

A second use of this technique is to increase the experiment sensitivity. In most of our field sweep measurement the fields step was 50G, or about 30kHz. The usual NMR line is presented as intensity vs. magnetic field, hence there is spacing of about 30kHz between the points. One possible way to increase the sensitivity is to measure in smaller steps in the field, but this will cost more experiment time. Another way is to use the fact that the frequency band width collected in our NMR is about 50kHz, and therefore there is some overlap between the data achieved in different fields in the frequency space. In this process we gain sensitivity of the Fourier space which can be tuned, and in my experiment is in the order of 1kHz.

We used this technique in order to separate the field sweep central transition peak into the different oxygen sites ingredients, which are shown in Fig. 3.1. After the translation into the frequency space it is also easier to fit the data: it becomes

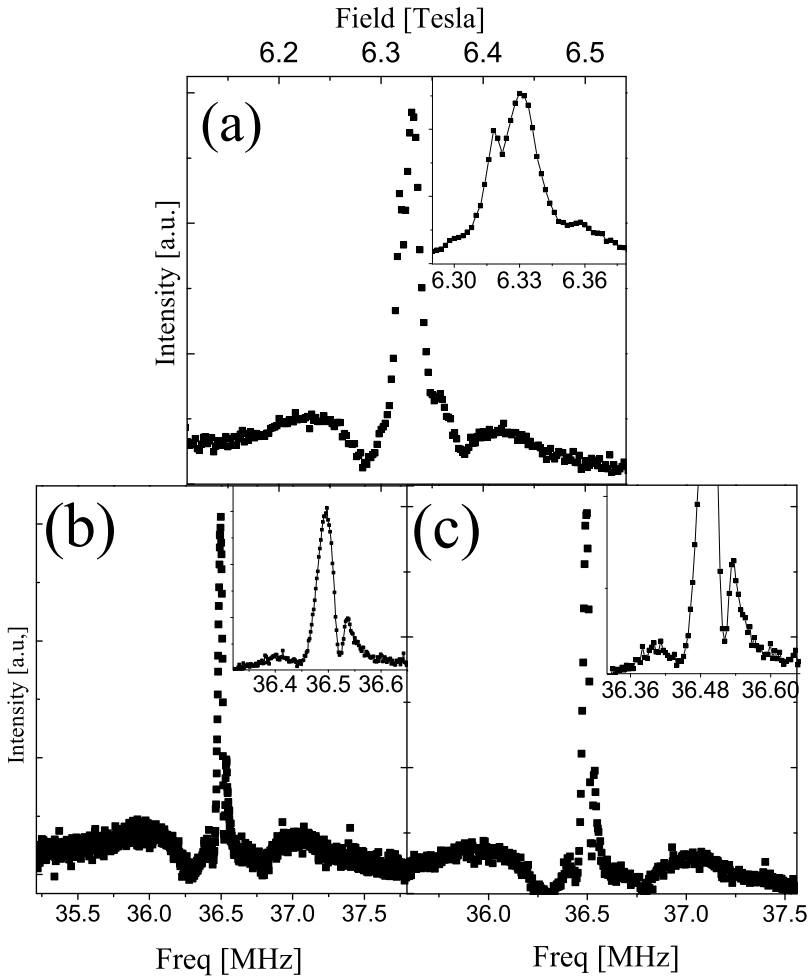

FIGURE 5.3: FSS of field sweep spectrum
Field sweep line of a sample (a) and the translation into the frequency space (b and c). In b and c different spacing are used in the Fourier transform. The method reconstructs Fig. 3.1.

eigenvalues problem instead of finding the correct parameter in the matrix for which a given eigenvalue is the solution.

5.3 Examination of the lanthanum signal

We observed that in many samples that the NMR field sweep line is not symmetric: The intensity of the low fields regime is bigger than the high fields regime. Originally we attributed this phenomenon to anisotropic shifts in the NMR Hamiltonian, σ_{aniso} and σ_{ax}, which are defined in section 2.3.1. In order to exam this assumption we performed experiments using different resonance frequency.

As explained in section 2.3.1, when we plot NMR line as a function of ppm from water most of the shifts do not depend on the working frequency. In contradiction, the NQR shift is not proportional to the working frequency and therefore changes as a function of the frequency (when ppm are used). Fig. 5.4 shows NMR line of the same sample taken at different frequencies. Since the correct way to translate our data into ppm requires translation into the frequency space (as explained in the previous part of the appendix) we present the data as a function of the external magnetic field. Arrows mark the translation of selected features to ppm.

We identify two peaks which do not move: the oxygen central transition (at 0 ppm) and a second peak at $-39 \cdot 10^3$ppm. Since the second peak does not depend on the working frequency it is not related to the NMR line of the oxygen. This shift matches the shift of a different nucleus: Lanthanum 139. These nuclei appear in the NMR line when the amount of ^{17}O is relatively low, which could be caused by reduction process or aging. The second option in demonstrated in Fig. 5.4: the two lines in the top figure were taken six months apart, and the ^{139}La signal becomes relatively stronger (the the signal of the central transition is normalized to 1). We observe this effect also in the isotope experiments (before the experiment we had more than 80% ^{18}O in the samples which reduced to slightly above 70%).

NMR line of a sample with $x = 0.4$ and $y = 7.08$ is presented in Fig. 5.5. The solid line is a theoretical fit to the oxygen line using Eq. 2.10. The inset shows the derivation from the theoretical line in the low fields regime, which indeed looks like

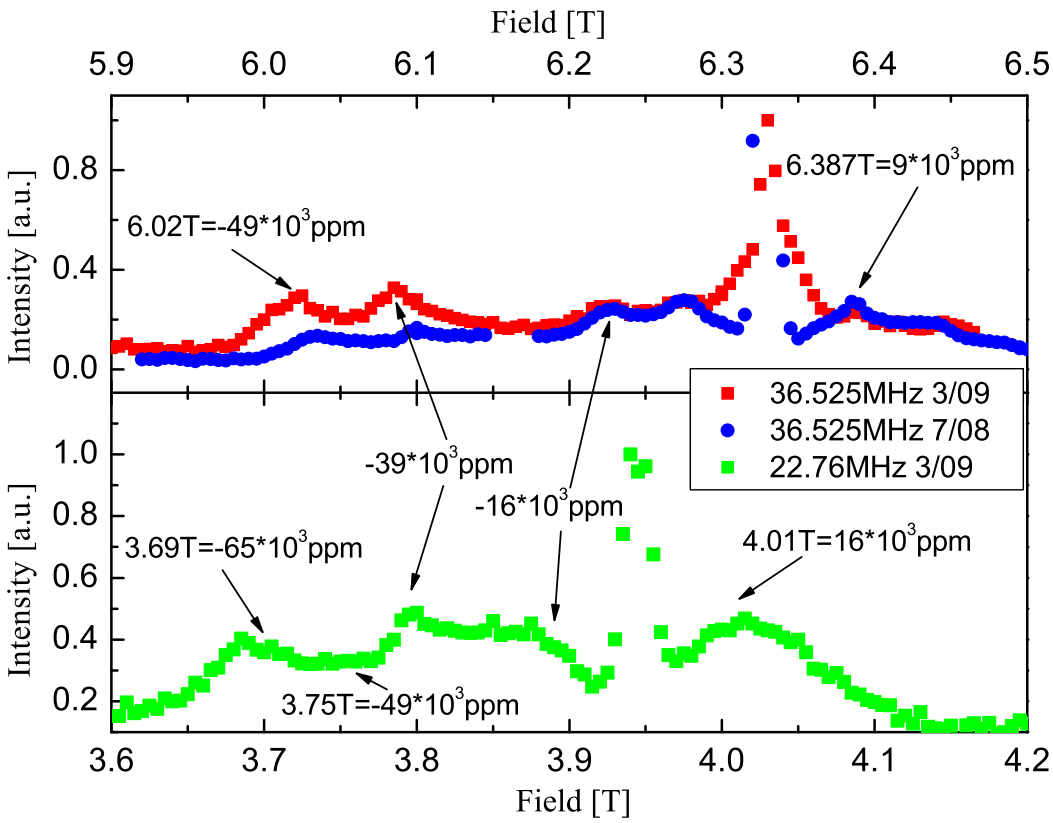

FIGURE 5.4: NMR lines at different frequencies
In the top panel the measurement frequency is 36.525MHz, in the bottom panel 22.76MHz. The data was taken at 110K for the same sample. Arrow identify the ppm of different line features with respect top the measurement frequency. Only two peaks do not change: the central transitions of the ^{17}O at 6.33T and the ^{139}La at about 6.1T.

NMR line- the ^{139}La line. When we measured samples without ^{17}O we got similar NMR lines. Since ^{139}La has a spin of 7/2 (which is difficult to fit) and it does not related to our research, we have not further investigated its NMR properties.

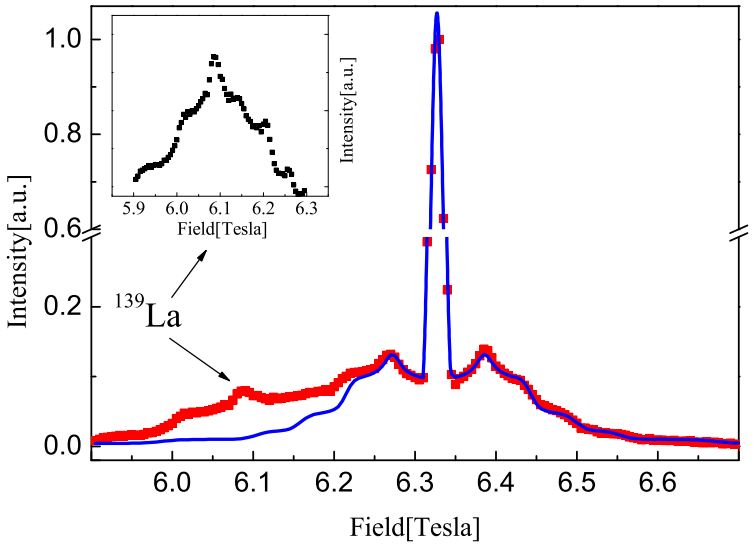

FIGURE 5.5: The ^{139}La peak
Raw data of an NMR measurement (red squares) and a fit to Eq. 2.10 (blue line). At low fields there is a deviation from the raw data due to the ^{139}La line. The difference between the raw data and the fit is presented in the inset.

Bibliography

[1] J. Bardeen, L. N. Cooper, and J. R. Schrieffer, Phys. Rev. B **108**, 1175 (1957).

[2] J. G. Bednorz and K. A. Müller, Z. Physik, B **64**, 189 (1986).

[3] A. Shilling *et al.*, Nature **363**, 56 (1993).

[4] Y. J. Uemura *et al.*, Phys. Rev. Lett. **62**, 2317 (1989).

[5] C. C. Homes *et al.*, Nature **430**, 539 (2004).

[6] T. Honma, and P. H. Hor, Phys. Rev. B **77**, 184520 (2008).

[7] A. Mourachkine, Jour. of Superconductivity **17**, 269 (2004).

[8] H. Zhou, Z. Ying, M. Cuoco, and C. Noce, arXiv:1002.4281v1.

[9] J. L. Tallon, Physica C **168**, 85 (1990).

[10] M.R. Presland *et al.*, Physica C **165**, 391 (1991).

[11] N. Nücker *et al.*, Phys. Rev. B **37**, 5158 (1988).

[12] F.C. Zhang and T. M. Rice, Phys. Rev. B **37**, 3759(R) (1988).

[13] J. Karpinski *et al.*, Phys. Rev. B **64**, 094518 (2001).

[14] R. Raimondi, J.H. Jefferson and L.F. Feiner, Phys. Rev. B **53**, 8774 (1996).

[15] D. Goldschmidt *et al.*, Phys. Rev. B **48**, 532 (1993).

[16] O. Chmaissem, Y. Eckstein, and C. G. Kuper, Phys. Rev. B **63**, 174510 (2001).

[17] J. Haase, O. P. Sushkov, P. Horsch, and G. V. M. Williams, Phys. Rev. B **69**, 094504 (2004).

[18] Y. Ando *et al.*, Phys. Rev. B **61**, 14956(R) (2000).

[19] S. Sanna *et al.*, EPL **86**, 67007 (2009).

[20] M. Ronay *et al.*, Solid State Comm. **77**, 699 (1991).

[21] R. Liang, D.A. Bonn and W.N. Hardy, Phys. Rev. B **73**, 180505(R) (2006).

[22] A. Kanigel *et al.*, Phys. Rev. Lett. **88**, 137003 (2002).

[23] R. Ofer *et al.*, Phys. Rev. B **74**, 220508(R) (2006).

[24] R. Ofer, A. Keren, O. Chmaissem and A. Amato, Phys. Rev. B **78**, 140508(R) (2008).

[25] Y. Lubashevsky and A. Keren, Phys. Rev. B **78**, 020505(R) (2008).

[26] Amit Keren, New J. Phys. **11** 065006 (2009).

[27] A. Keren, A. Kanigel, and G. Bazalitsky, Phys. Rev. B. **74**, 172506 (2006).

[28] E. Maxwell, Phys. Rev. **78**, 477 (1950).

[29] C. A. Reynolds, B. Serin, W. H. Wright, and L. B. Nesbitt, Phys. Rev. **78**, 487 (1950).

[30] R. Khasanov *et al*, Phys. Rev. Lett. **101**, 077001 (2008).

[31] D. J. Pringle, G. V. M. Williams, and J. L. Tallon, Phys. Rev. B **62**, 12527 (2000).

[32] H. Keller, Springer-Verlag Berlin Heidelberg 2005.

[33] Gou-meng Zhao, K. K. Singh and D. E. Morris, Phys. Rev. B **50**, 4112 (1994).

[34] A. Bill, V.Z. Kresin, and S.A. Wolf, cond-mat/9801222.

[35] E. Schachinger, M. G. Greeson, and J. P. Carbotte, Phys. Rev. B **42**, 406 (1990).

[36] Daniel S.Fisher *et al.*, Phys. Rev. Lett **61**, 482 (1988).

[37] V.Z. Kresin and S.A. Wolf, Phys. Rev. B **49**, 3652(R) (1994).

[38] M. Serbyn and P. A. Lee, cond-mat/1009.2429.

[39] E.H. Appelman *et al.*, Inorg. Chem **26**, 3237 (1987).

[40] C. P. Slichter, *Principles of Magnetic Resonance* (Harper and Row, New York, 1963).

[41] E. Fukushima and S. Roeder, *Experimental Pulse NMR* (Addison-Wesley, 1981).

[42] A. Abragam, *Principles of Nuclear Magnetism* (Oxford Science Publications, 2006).

[43] J. F. Baugher, P. C. Taylor, T. Oja, and P. J. Bray, Jour. of Chem. Phys. **50**, 4914 (1969).

[44] W. G. Clark, M. E. Hanson and F. Lefloch, Rev. Sci. Instrum. **66**, 2453 (1995).

[45] *Muon Science*, IProceedings of the Fifty First Scottish Universities Summer School in Physics, St Andrews, August 1998.

[46] M. Shay *et al.*, Phys. Rev. B **80**, 144511 (2009).

[47] E. Oldfield *et al.*, Phys. Rev. B **40**, 6832 (1989).

[48] M. Takigawa *et al.*, Phys. Rev. B **43**, 247 (1991).

[49] P. C. Hammel *et al.*, Phys. Rev. Lett **63**, 1992 (1989).

[50] W. W. Warren *et al.*, Phys. Rev. Lett **62**, 1193 (1989).

[51] I. Tomeno *et al.*, Phys. Rev. B **49**, 15327 (1994).

[52] T. Timusk and B. Statt, Reports on Progress in Physics **62**, 61 (1999).

[53] E. Amit and A. Keren, Phys. Rev. B **84**, 172509 (2010).

חקר על-מוליכות

באמצעות איזוטופים של חמצן

ערן עמית

חקר על-מוליכות

באמצעות איזוטופים של חמצן

חיבור על מחקר

לשם מילוי חלקי של הדרישות לקבלת לקבלת

תואר דוקטור לפילוסופיה

ערן עמית

הוגש לסנט הטכניון- מכון טכנולוגי לישראל

שבט תשע"א חיפה ינואר 2011

תקציר

מוליכות העל בטמפרטורות גבוהות התגלתה במוליכי העל הנחושתיים בשנות השמונים של המאה העשרים. מאז גילוי חומרים אלו הושקעו מאמצים רבים, הן ניסוניים והן תיאורטיים, להבין את המנגנון שאחראי לתופעה זו. לעשרות החומרים השונים שמשתייכים לקטגורית מוליכי העל הנחושתיים תכונות משותפות רבות, דבר המרמז על כך שבכולן מתרחש אותו תהליך פיסיקלי. אחד האתגרים בחומרים אלו הוא זיהוי התכונות הרלוונטיות למוליכות העל מתוך שלל המאפיינים הכימיים והפיסיקלים. בעבודה זו אנו מנסים לזהות תכונות אלו על ידי מדידת התגובה של חומרים לשינוים קטנים בהרכבם הכימי. אנו מראים שאלו אכן הפרעות קטנות, ולכן ניתן לתאר את התוצרים באמצעות שינויים קטנים של פרמטרים בהמילטוניאן. בחלק הראשון של עבודה זו אנו משווים בין ערכי האילוח הקריטים של חומרים שונים. תכונותיהם הפיסיקליות של מוליכי העל הנחושתיים ניתנים לשינוי באמצעות שינוי מספר החורים (אילוח). מצב היסוד של חומרים אלו הוא אנטיפרומגנטי: הספינים האלקטרונים של אטומי הנחושת הסמוכים מסודרים בכיוונים הפוכים. כאשר מוסיפים חורים למישורים העל מוליכים טמפרטורת המעבר לפאזה יורדת ובהמשך נעלמת, ומצב היסוד של החומר הופך לזכוכיתי: סדר אנטיפרומגנטי קצר טווח. גם טמפרטורת המעבר לפאזה הזכוכיתית יורדת כאשר מוסיפים חורים , ולבסוף נעלמת.

לאחר אילוח מספק של החומר מצב היסוד הוא מוליכות על. התלות של טמפרטורת המעבר לפאזה זו במספר החורים נראית כקשת בעלת ערך מכסימלי המאפיין את החומר (טמפרטורת מעבר מכסימלית לפאזה העל מוליכה). בפאזה העל מוליכה השדות החשמלים והמגנטים בתוך

החומר הם אפס. במוליכי העל הנחושתיים קיימות פאזות נוספות בטמפרטורות גבוהות אך הן לא רלוונטיות למחקר זה.

אנו מגדירים את ערכי האילוח הקריטים ככמויות החורים הדרושות על מנת לשנות את מצב היסוד של החומר. אנחנו משווים ערכים אלו עבור שני חומרים:

$(Ca_xLa_{1-x})(Ba_{1.75-x}La_{0.25+x})Cu_3O_7$ (CLBLCO) עם $x=0.1$ ו-$x=0.4$. בתא היחידה של חומרים אלו שני מישורים של CuO_2, המישורים העל מוליכים, ומישור שלישי, המכיל נחושות וחמצנים, שאת כמות החמצנים בו ניתן לשנות.

בין כל שני מישורים קיים אתר המאוכלס על ידי קטיונים. הרכב הקטיונים נקבע על ידי הפרמטר x מהנוסחא המולקולרית. ככל שמגדילים את x המטען הקטיוני הממוצע בין המישורים העל מוליכים קטן, אך סך כל המטען הקטיוני איננו משתנה (על פי רמות החמצון הידועות שלהם).

חומרים אלו מואלחים על ידי שינוי מספר החמצנים בתא היחידה (הוספת חמצנים למישור השלישי) המוגדרים על ידי הפרמטר y. הוספת חמצנים מגדילה את מספר החורים באורביטלה האלקטרונית הקושרת של החמצנים במישור, $2p_\sigma$. אנחנו משווים ישירות את מספר החורים הללו בחומרים שונים באמצעות מדידות תהודה מגנטית של האיזוטופ חמצן 17. השכיחות של איזוטופ זה מכלל החמצן באטמוספרה היא פחות מ- 0.04%, ולכן לפני המדידות אנחנו מעשירים את הדגמים באיזוטופ.

תהודה מגנטית גרעינית של גרעין בעל מומנט קוואדרופולי כמו חמצן 17 מספקת מידע על השדות החשמלים והמגנטים מסביב לגרעין. מפני שהשדה החשמלי נוצר מהתפלגות המטענים מסביב לגרעין ניתן ללמוד מהמדידה על כמות האלקטרונים (או החורים) הסובבים את הגרעין. השינוי העיקרי בשדות החשמלים שחש גרעין החמצן במישור העל מוליך עקב אילוח נגרם משינוי בכמות האלקטרונים (או יצירת חורים) באורביטלת החמצן הקושרת. אנו משתמשים בכך ובסימטריות הדומות של החומרים כדי לבצע מדידות מדויקות של מספר החורים.

בניסוי תהודה מגנטית גרעינית שמים את הדגם בשדה מגנטי חזק (ובמקרה שלנו בטמפרטורה של 110 קלווין). השדה המגנטי יוצר מומנט מגנטי גרעיני בדגם, במקביל לכיוון השדה החיצוני. מומנט זה מכיל את המידע על הסביבה החשמלית והמגנטית של הגרעין. בכדי למדוד אותו מפעילים לזמן קצר שדה בכיוון ניצב לשדה החזק, בתדירות התהודה של המומנט. עקרון התהודה גורם לכך שהמומנט יסתובב מסביב לשדה החלש יותר. כאשר מגיעים לזווית של כתשעים מעלות בין המומנט לשדה החזק מכבים את השדה החלש. כעת המומנט המגנטי חש רק את השדה המגנטי הסטטי הניצב לו- ולכן מתחיל להסתובב סביבו. מומנט מגנטי מסתובב יוצר שטף מגנטי (חוק פאראדי), שאותו מודדים באמצעות הזרם המושרה בסליל שמקיף את הדגם.

ההשוואה בין כמויות החורים בתלות באילוח ובפרמטר x מראה שלמרות שמתקבלים ערכי אילוח קריטים שונים בתלות בפרמטר y, ערכים אלו זהים בתלות במספר החורים.

בחלקה השני של העבודה אנו מודדים את ההשפעה של החלפת איזוטופים של חמצן על טמפרטורת המעבר לפאזה האנטיפרומגנטית. אחד הניסויים שתרמו רבות להבנת מנגנון מוליכות העל בחומרים קונבנציונלים היה מדידת טמפרטורת המעבר לפאזה העל מוליכה בתלות במסת היסוד על ידי שימוש באיזוטופים. ככלל, לשימוש באיזוטופים שונים אמור להיות השפעה קטנה על תכונות החומר. השינוי היחידי הוא במסת הגרעין ולא במטענו או בכמות האלקטרונים הסובבים אותו, ולכן ניתן לצפות שההשפעה העיקרית תהיה על תנועות הגרעין. במצב מעובה תנודות הגרעין הקולקטיביות מתוארות על ידי פונונים, ואכן בתאוריה למוליכות על קונבנציונלית האפקט האיזוטופי מוסבר על ידי תפקיד הפונונים במוליכות העל. במוליכי העל הנחושתיים המצב מסובך בהרבה מפני שהם מורכבים ממספר יסודות ומפני שהם ניתנים לאילוח. במדידות של מוליכי על נחושתיים נמצא כי השפעת החלפת האיזוטופים על טמפרטורת המעבר לפאזה העל מוליכה תלויה ברמת האילוח. ישנן תאוריות שונות שמנסות להסביר תופעה זו. מדידת האפקט האיזוטופי בפאזה האנטיפרומגנטית יכולה לעזור לאשש או לפסול נסיונית חלק מתאוריות אלו.

אנחנו משתמשים בחומר $(Ca_{0.1}La_{0.9})(Ba_{1.65}La_{0.35})Cu_3O_7$ כי עבורו קיים תחום בדיארגמת הפאזות בו טמפרטורה זו אינה תלויה בכמות החורים. אנו מוצאים כי בתחום זה החלפת האיזוטופים איננה משפיעה על הטמפרטורה הקריטית.

בניסויים בחלק זה של העבודה אנו משתמשים במיואונים. אנו יורים קרן של מיואונים בעלי ספין בכיוון אחיד לתוך הדגם. ספין של מיואון שמרגיש שדה מגנטי בדגם יסתובב בתדירות לרמור, ולכן ממדידת כיוון הספין המיואוני הממוצע בתלות בזמן ניתן ללמוד על הסדר המגנטי של החומר. כדי למדוד את כיוון הספין אנו משתמשים בזמן החיים הקצר יחסית של מיואון: לאחר 2.2 מיליוניות השניה הוא דועך לפוזיטרון, שעף בכיוון אליו הצביע ספין המיואון בזמן הדעיכה. אנו מודדים את הפוזיטרונים, מסיקים מה היה הספין המיואוני, וממנו-אם בחומר יש סדר מגנטי או שהוא בפאזה שאיננה מגנטית. ממדידות בטמפרטורות שונות ניתן למצוא את טמפרטורת מעבר הפאזה בדיוק של עשיריות קלווין.

המסקנה הראשונה מעבודה זו היא שערכי האילוח הקריטיים אינם תלויים בחומר כאשר משתמשים בפרמטר הפיסיקלי הנכון- כמות החורים באורביטלה הקושרת של החמצן. השלכה ראשונה למסקנה זו היא שכאשר מודדים שינויים קטנים בדיאגרמות הפאזות חובה להשתמש בפרמטר זה, אחרת ניתן לשייך תופעות שונות לעובדה הפשוטה שכמות החורים איננה זהה. אנחנו חושבים שזה המקרה במדידות שדווחו בעבר על מדידת האפקט האיזוטופי במוליכי על נחושתיים: האפקט המרכזי היה שינוי במספר החורים ולא בתכונות אחרות של החומר.

השלכה נוספת של הממצא הנ"ל היא שכעת אנו מבינים טוב יותר את החומרים השונים השייכים ל CLBLCO. באמצעות שימוש בגדלים מדידים בלבד אנחנו יכולים לצייר דיאגרמת פאזות משותפת לחומרים השונים. בתהליך זה אנו מוצאים כי סקלת האנרגיה המגדירה את טמפרטורת המעבר המכסימלית לפאזת מוליכות העל של חומר מסויים היא עוצמת הצימוד האנטיפרומגנטי בחומר שאיננו מאולח.